



Dear Author:

Thank you for publishing with AGU. Your proofs are attached. Following the annotation guidelines and returning the proofs quickly will allow prompt online posting of the final version of your paper.

You will notice a few differences in the proofs starting in 2019. We have updated our logos and headers to highlight AGU's Centennial. In addition, the PDF version now is rendered in a new serif font—[Stix](#)—designed to optimize display of math, equations, and scientific notation. We have added several new features to the journal website as well.

There are various ways in which you can promote and share your work, both while the final version of the article is being prepared by Wiley and once it has been published. For suggestions, please see our [resource page](#). The online version of your paper includes [Altmetrics](#), which continually tracks and links to mentions in the media, blogs and social media. Links to scholarly citations are also provided in the online PDF version.

If you have not already, we encourage you to create an ORCID (Open Researcher and Contributor ID) so that your work can be uniquely tracked. Your ORCID can be created and linked through your GEMS account.

Finally, your feedback is important to us. We will also be contacting you soon after your article is published with an author survey. Please take a few minutes to respond as your input is important in improving the overall editorial and production process. If you have questions or comments regarding your AGU Publications experience, including information on production and proofs, please contact us any time at publications@agu.org. Thank you again for supporting AGU.

Sincerely,

A handwritten signature in blue ink that reads 'Matt Giampoala'.

Matt Giampoala, VP Publications, AGU

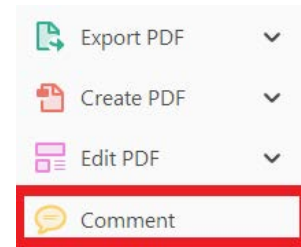
USING e-ANNOTATION TOOLS FOR ELECTRONIC PROOF CORRECTION

Required software to e-Annotate PDFs: Adobe Acrobat Professional or Adobe Reader (version 11 or above). (Note that this document uses screenshots from Adobe Reader DC.)


The latest version of Acrobat Reader can be downloaded for free at: <http://get.adobe.com/reader/>

Once you have Acrobat Reader open on your computer, click on the Comment tab (right-hand panel or under the Tools menu).


This will open up a ribbon panel at the top of the document. Using a tool will place a comment in the right-hand panel. The tools you will use for annotating your proof are shown below:

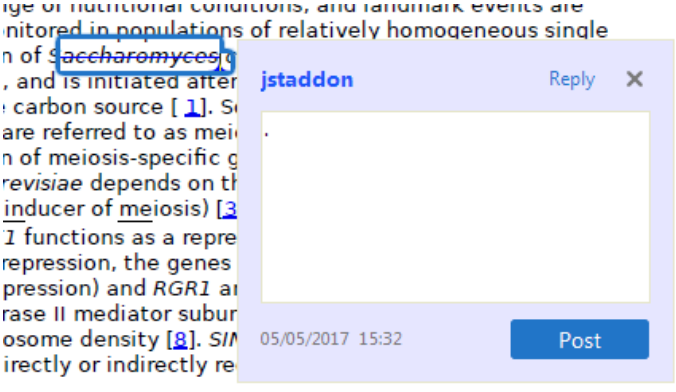


1. Replace (Ins) Tool – for replacing text.


 Strikes a line through text and opens up a text box where replacement text can be entered.

How to use it:

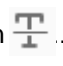
- Highlight a word or sentence.
- Click on .
- Type the replacement text into the blue box that appears.



2. Strikethrough (Del) Tool – for deleting text.

 Strikes a red line through text that is to be deleted.



How to use it:

- Highlight a word or sentence.
- Click on .
- The text will be struck out in red.



experimental data if available. For ORFs to be had to meet all of the following criteria:

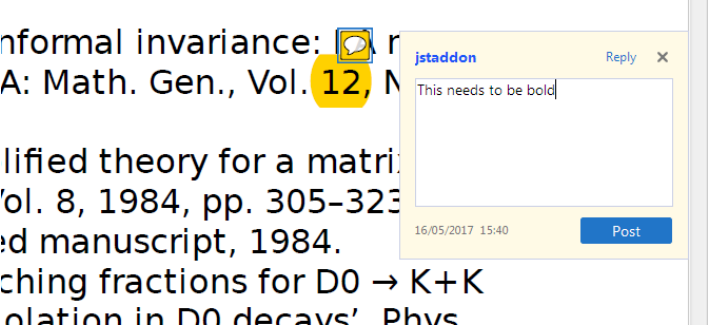
1. Small size (35-250 amino acids).
2. Absence of similarity to known proteins.
3. Absence of functional data which could not be the real overlapping gene.
4. Greater than 25% overlap at the N-terminus terminus with another coding feature; over both ends; or ORF containing a tRNA.


3. Commenting Tool – for highlighting a section to be changed to bold or italic or for general comments.

  Use these 2 tools to highlight the text where a comment is then made.


How to use it:

- Click on .
- Click and drag over the text you need to highlight for the comment you will add.
- Click on .
- Click close to the text you just highlighted.
- Type any instructions regarding the text to be altered into the box that appears.




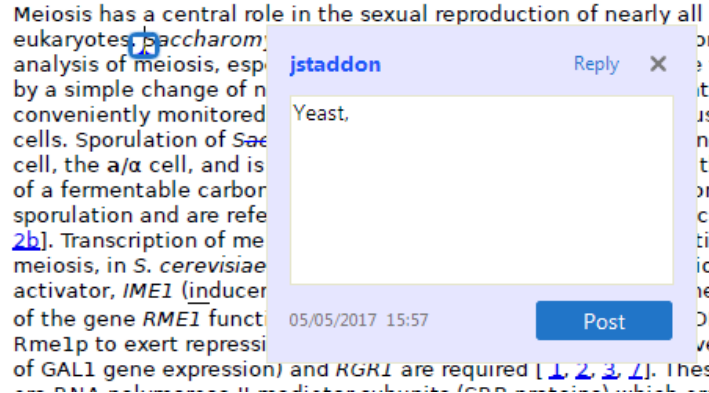
informal invariance:  r
A: Math. Gen., Vol. 12, N
simplified theory for a matrix
Vol. 8, 1984, pp. 305-323
ed manuscript, 1984.
changing fractions for $D_0 \rightarrow K+K$
relation in D_0 decays' Phys

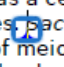
4. Insert Tool – for inserting missing text at specific points in the text.

 Marks an insertion point in the text and opens up a text box where comments can be entered.


How to use it:

- Click on .
- Click at the point in the proof where the comment should be inserted.
- Type the comment into the box that appears.




Meiosis has a central role in the sexual reproduction of nearly all eukaryotes.  *Saccharom* analysis of meiosis, especially by a simple change of conveniently monitored cells. Sporulation of *Sac* cell, the a/α cell, and is of a fermentable carbon sporulation and are referred to [2b]. Transcription of meiosis, in *S. cerevisiae* activator, *IME1* (inducer of the gene *RME1* function of *Rme1p* to exert repression of GAL1 gene expression) and *RGR1* are required [1, 2, 3, 4]. These genes are DNA-dependent RNA polymerase II-mediated subunits (RNAP II) which are

5. Attach File Tool – for inserting large amounts of text or replacement figures.

 Inserts an icon linking to the attached file in the appropriate place in the text.


How to use it:

- Click on .
- Click on the proof to where you'd like the attached file to be linked.
- Select the file to be attached from your computer or network.
- Select the colour and type of icon that will appear in the proof. Click OK.


The attachment appears in the right-hand panel.

chondrial preparator
ative damage injury
re extent of membra
i, malondialdehyde (TBARS) formation.
used by high perform

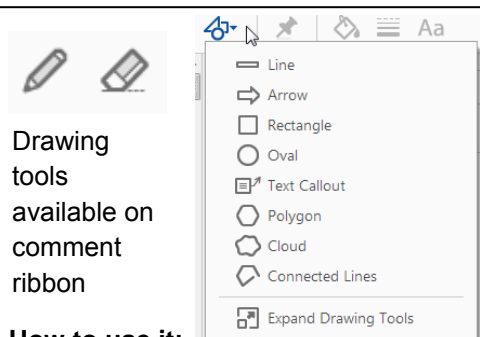
6. Add stamp Tool – for approving a proof if no corrections are required.

 Inserts a selected stamp onto an appropriate place in the proof.

How to use it:

- Click on .
- Select the stamp you want to use. (The **Approved** stamp is usually available directly in the menu that appears. Others are shown under *Dynamic*, *Sign Here*, *Standard Business*).
- Fill in any details and then click on the proof where you'd like the stamp to appear. (Where a proof is to be approved as it is, this would normally be on the first page).

of the business cycle, starting with the
on perfect competition, constant ret
production. In this environment goods
extra costs should be set to market
he market is determined by the model. The New-Key
otaki (1987), has introduced produc
general equilibrium models with nomin
and downward sloping. Most of this literat

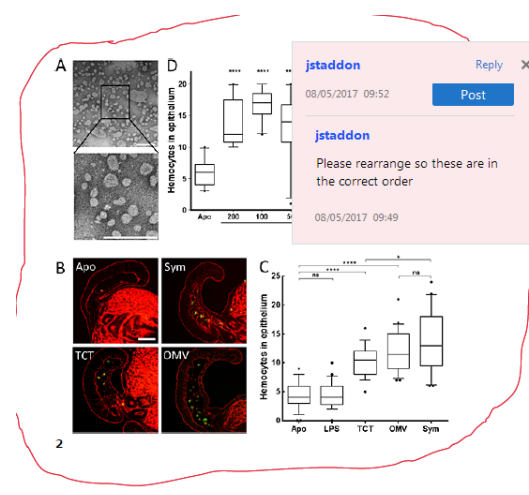


How to use it:

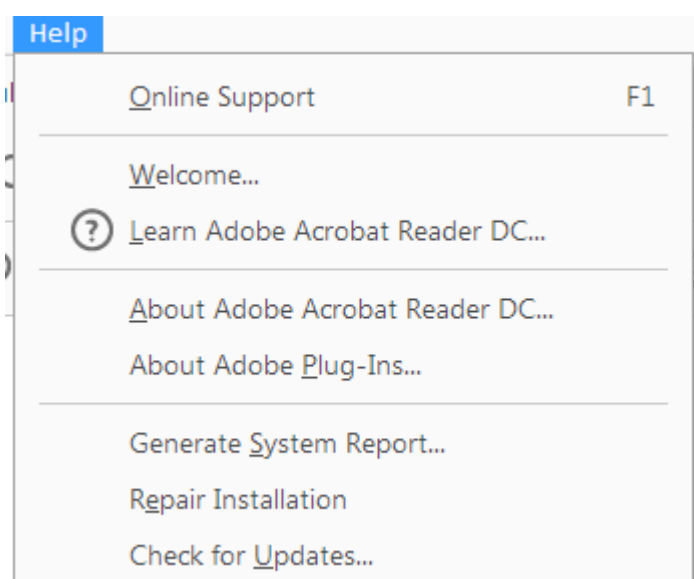
- Click on one of the shapes in the **Drawing Markups** section.
- Click on the proof at the relevant point and draw the selected shape with the cursor.
- To add a comment to the drawn shape, right-click on shape and select *Open Pop-up Note*.
- Type any text in the red box that appears.

7. Drawing Markups Tools – for drawing shapes, lines, and freeform annotations on proofs and commenting on these marks.

Allows shapes, lines, and freeform annotations to be drawn on proofs and for comments to be made on these marks.



For further information on how to annotate proofs, click on the **Help** menu to reveal a list of further options:



**PLEASE COMPLETE THE PUBLICATION FEE CONSENT FORM BELOW
AND
RETURN TO THE PRODUCTION EDITOR WITH YOUR PROOF CORRECTIONS**

Please return this completed form and direct any questions to the Wiley Journal Production Editor at JGRBprod@wiley.com.

To order OnlineOpen, you must complete the OnlineOpen order form at:

https://authorservices.wiley.com/bauthor/onlineopen_order.asp

Authors who select OnlineOpen will be charged the standard OnlineOpen fee for your journal, but excess publication fees will still apply, if applicable. **If your paper has generated excess publication fees, please complete and return the form below in addition to completing the OnlineOpen order form online (excess fees are billed separately).** If you would like to choose OnlineOpen and you have not already submitted your order online, please do so now.

YOUR ARTICLE DETAILS

Journal: *Journal of Geophysical Research: Solid Earth*

Article: Albano, M., Barba, S., Saroli, M., Polcari, M., Bignami, C., Moro, M., Stramondo, S., & Di Bucci, D. (2019). Aftershock rate and pore fluid diffusion: Insights from the Amatrice-Visso-Norcia (Italy) 2016 seismic sequence. *Journal of Geophysical Research: Solid Earth*, 124. <https://doi.org/10.1029/2018JB015677>

OnlineOpen: No **Words:** 9,481 **Tables:** 1 **Figures:** 9 **Total Publishing Units:** 29

Journal Base Fee: \$1,000
Excess Publishing Units: 4@ \$125 \$500
Publication Fee Total: USD \$1,500

Please provide the information requested below.

Bill to:

Name: _____
Institution: _____
Address: _____
Phone: _____ **Email:** _____
Signature: _____ **Date:** _____

An invoice will be mailed to the address you have provided once your edited article publishes online in its final format. Please include on this publication fee form any information that must be included on the invoice.

Publication Fees and Length Guidelines:
<http://publications.agu.org/author-resource-center/>

Frequently Asked Billing Questions:
[http://onlinelibrary.wiley.com/journal/10.1002/\(ISSN\)2169-8996/homepage/billing_faqs.pdf](http://onlinelibrary.wiley.com/journal/10.1002/(ISSN)2169-8996/homepage/billing_faqs.pdf)

Purchase Order Instructions:
 Wiley must be listed as the contractor on purchase orders to prevent delay in processing invoices and payments.

Author Query Form

Journal: Journal of Geophysical Research: Solid Earth








Article: jgrb_53211

Dear Author,


During the copyediting of your paper, the following queries arose. Please respond to these by annotating your proofs with the necessary changes/additions.

- If you intend to annotate your proof electronically, please refer to the E-annotation guidelines.
- If you intend to annotate your proof by means of hard-copy mark-up, please use the standard proofing marks. If manually writing corrections on your proof and returning it by fax, do not write too close to the edge of the paper. Please remember that illegible mark-ups may delay publication.

Whether you opt for hard-copy or electronic annotation of your proofs, we recommend that you provide additional clarification of answers to queries by entering your answers on the query sheet, in addition to the text mark-up.

Query No.	Query	Remark
Q1	AUTHOR: Please fill out the Publication Fee Consent Form in these proofs (including complete mailing address) and return to the Production Editor with your proofs.	
Q2	AUTHOR: Please verify that the linked ORCID identifiers are correct for each author.	
Q3	AUTHOR: Please confirm that forenames/given names (blue) and surnames/family names (vermilion) have been identified correctly.	
Q4	AUTHOR: Tung & Masterlark, 2018 does not appear in the reference list. Please add to the reference list or delete from text.	
Q5	AUTHOR: Please note that your references and their citations have been edited according to APA/AGU style, available here.	
Q6	AUTHOR: "Tung & Masterlark, 2018a" has not been cited in the text. Please indicate where it should be cited; or delete from the Reference List.	
Q7	AUTHOR: "Tung & Masterlark, 2018b" has not been cited in the text. Please indicate where it should be cited; or delete from the Reference List.	

Please confirm that the funding sponsor list below was correctly extracted from your article: that it includes all funders and that the text has been matched to the correct FundRef Registry organization names. If a name was not found in the FundRef registry, it may not be the canonical name form, it may be a program name rather than an organization name, or it may be an organization not yet included in FundRef Registry. If you know of another name form or a parent organization name for a "not found" item on this list below, please share that information.

FundRef Name	FundRef Organization Name
FISR 2016 research project	not found 

JGR Solid Earth

RESEARCH ARTICLE

10.1029/2018JB015677

Key Points:

- A quick evaluation of the pore pressure contribution to the aftershock release after the August 2016 Amatrice earthquake has been performed
- Poroelastic modeling shows that the postseismic fluid flow diffusion is related to the daily aftershock rates
- Early information and data are useful in developing a model to describe the approximate temporal evolution of overpressured conditions

Supporting Information:

- Supporting Information S1

Correspondence to:

M. Albano,
matteo.albano@ingv.it

Citation:

Albano, M., Barba, S., Saroli, M., Polcari, M., Bignami, C., Moro, M., Stramondo, S., & Di Bucci, D. (2019). Aftershock rate and pore fluid diffusion: Insights from the Amatrice-Visso-Norcia (Italy) 2016 seismic sequence. *Journal of Geophysical Research: Solid Earth*, 124. <https://doi.org/10.1029/2018JB015677>

Received 20 FEB 2018

Accepted 21 DEC 2018

Accepted article online 28 DEC 2018

Aftershock Rate and Pore Fluid Diffusion: Insights From the Amatrice-Visso-Norcia (Italy) 2016 Seismic Sequence

Matteo Albano¹ , Salvatore Barba¹ , Michele Santucci^{2,1} , Marco Polcari¹ , Christian Bignami¹ , Marco Moro¹, Salvatore Stramondo¹ , and Daniela Di Bucci³ 

¹Istituto Nazionale di Geofisica e Vulcanologia, Rome, Italy, ²Dipartimento di Ingegneria Civile e Meccanica, Università degli Studi di Cassino e del Lazio meridionale, Cassino, Italy, ³Dipartimento della Protezione Civile Italiana, Rome, Italy

Abstract We developed a numerical model by using only early and unreviewed data and information related to the 2016 M_w 6 earthquake in central Italy to quickly evaluate the pore pressure contribution to the aftershock release after a severe mainshock. Moreover, a computational procedure is proposed for discussing if and how such an approach could be useful in the management of a seismic crisis. The two-dimensional finite element model in this study is based on poroelastic theory and includes a planar seismogenic fault. The model geometry and parameters are based on data collected from the literature before the mainshock. The dip and depth of the seismogenic fault are based on preliminary information from focal mechanisms and related fault inversions. The fault slip is calibrated with synthetic aperture radar interferometric data, and the hydraulic properties of the medium are progressively calibrated based on routine aftershock data collected during the sequence. The procedure proposed here can be efficiently applied in a diverse range of cases depending on data availability. Typically, the available “ingredients” allow for a quick, simplified analysis to be conducted rapidly. The simulation results show that early information and routine data are useful in developing and calibrating a model that can rapidly describe the approximate temporal evolution of overpressured conditions, which represent a crucial driving mechanism in the occurrence of aftershocks. These findings highlight the need to adequately consider time-dependent poroelastic effects when modeling postseismic scenarios and predicting the spatiotemporal evolution of the stresses following a large earthquake.

1. Introduction

Because the vulnerability of buildings increases after a large quake, strong aftershocks constitute a significant risk factor that must be evaluated and managed. Occasionally, the energy of aftershocks is comparable to or even larger than that of the mainshock (Ammon et al., 2008; Lay & Kanamori, 1980; Scognamiglio et al., 2012). Such events are referred to as earthquake doublets or triplets (Utsu, 2002), and they may produce additional damage and casualties, as in case of the Emilia-Romagna (Italy) 2012 seismic sequence (Scognamiglio et al., 2012). The management of a seismic crisis could benefit from aftershock forecasts.

Traditional forecasting methods (Gerstenberger et al., 2005; Ogata, 1998; Reasenber & Jones, 1989) describe the spatial and temporal statistical distributions of aftershocks. However, these statistical models could be improved by incorporating knowledge of the seismogenic process and fault interactions.

Although the spatial distribution of aftershocks usually correlates well with the coseismic static Coulomb stress, the time delay of the aftershocks needs to be described with a time-dependent physical mechanism. Different time-dependent physical mechanisms may account for the observed time delay of aftershocks, including afterslip (Bürgmann et al., 2002), rate and state friction (Dieterich, 1972), viscoelastic relaxation (Bürgmann & Dresen, 2008), and poroelastic rebound (Jónsson et al., 2003; Tung et al., 2018). In particular, pore fluid diffusion correlates with the aftershock decay rate (Booker, 1974; Nur & Booker, 1972), and changes in postseismic pore pressure significantly influence crustal stresses in the first few months after a strong earthquake. Poroelastic stress changes well explain both the temporal and spatial distributions of the majority of aftershocks (Albano et al., 2017; Antonioli et al., 2005; Bosl & Nur, 2002; Hughes et al., 2010; Nur & Booker, 1972; Tung & Masterlark, 2018; Tung et al., 2018). These observations suggest that poroelastic stress changes are a significant driving mechanism for aftershock nucleation in fractured crusts. Accordingly, studying the fluid diffusion process could lead to improvements in the modeling of fault

1
2
3
4
5
6
7
8
9
10
11
12
13
14
15
16
17
18
19
20
21
22
23
24
25
26
27
28
29
30
31
32
33
34
35
36
37
38
39
40
41
42
43
44
45
46
47
48
49
50
51
52
53
54
55
56
57
58
59
60
61
62
63
64
65
66

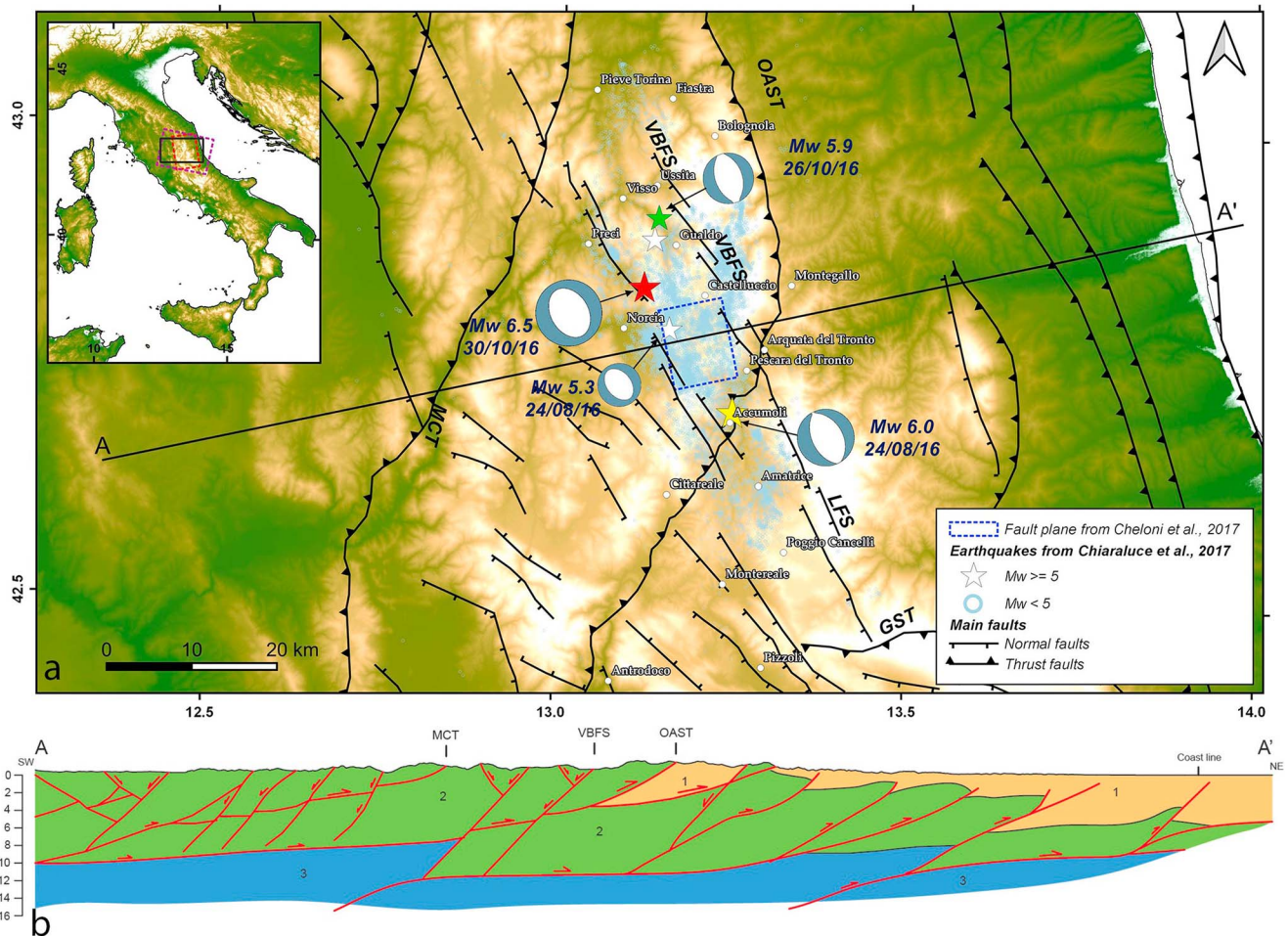


Figure 1. (a) Tectonic sketch of the study area (black rectangle in the inset figure) and earthquakes recorded from 24 August to 30 October 2016 (Chiaraluce et al., 2017). Blue dots: earthquakes with $M_w > 1.5$. Stars: earthquakes with $M_w > 5.0$. The yellow star indicates the 24 August 2016 event. The green and red stars indicate the 26–30 October 2016 events. The tectonic framework is depicted by the thrusts of Olevano-Antrodoco-Sibillini Mountains (OAST), Mt. Cavallo (MCT), and Gran Sasso (GST) and by the normal faults of Mt. Vettore-Mt. Bove (VBFS) and Laga (LFS) systems (Lavecchia et al., 1994; Pizzi et al., 2002; Pizzi & Galadini, 2009). The dashed polygons in the inset figure indicate the footprint of the ascending (red) and descending (violet) Sentinel-1 synthetic aperture radar frames. (b) Simplified geological section along the A–A' profile in (a) (Calamita et al., 2000; Lavecchia et al., 1994). The geologic units are grouped as follows: (1) continental and foredeep terrigenous deposits (Quaternary–Miocene); (2) pelagic carbonate succession (Jurassic–Oligocene); and (3) crystalline basement, topped by anhydrite and dolomite deposits (up to Middle–Upper Triassic).

interactions after strong earthquakes, thereby strengthening traditional forecasting methods. Complex numerical poroelastic models provide trustworthy results on fluid diffusion but require a long construction time and high computational costs, and they can only be used a posteriori to investigate the seismic sequence with more detail. Forecasting methods must provide reproducible results in a relatively short time. A first-order model is easily replicable and can rapidly assess the timing and location of aftershocks immediately after a strong earthquake. The first-order model must carry essential information about the studied area and the involved parameters without overparametrizing the problem, and it must be incrementally refined in successive steps based on the availability of new data in the days or weeks after the first event. Such a model must be able to provide results compatible to those obtained from complex and more detailed models, made a posteriori. Such an approach is required to understand if an oversimplification of a detailed ex post refined model can also provide useful insights about the aftershock sequence within a short time period.

As a case study, we considered the Amatrice-Visso-Norcia 2016 seismic sequence. On 24 August 2016, a M_w 6.0 earthquake struck central Italy (Figure 1a) and caused 299 casualties and severe damage to the towns of P13 Accumoli and Amatrice (Chiaraluce et al., 2017). On the same day, a second large event (M_w 5.3) struck a few

kilometers to the northwest (Figure 1a). Hundreds of aftershocks were recorded, with the daily number of events approximately constant for the first 10 days (Figure S1a in the supporting information). Aftershocks migrated gradually from the earthquake epicenter, suggesting a possible diffusive transient process (Chiaraluce et al., 2017; Tung & Masterlark, 2018; Walters et al., 2018). Nearly 2 months later (26 October), a M_w 5.9 earthquake nucleated farther to the north between the towns of Ussita and Visso (Figure 1a). After 4 days (30 October), a M_w 6.5 earthquake, the largest in the sequence, struck the town of Norcia and caused further damage and building collapse. The three largest shocks produced an increase in the water level in wells at distances of more than 100 km from the epicentral area (Barberio et al., 2017). As of December 2017, the sequence included more than 80,000 events with magnitudes of up to M_w 5 (Chiaraluce et al., 2017; ISIDE Working Group, 2016). The moment tensor solutions for the most significant events display a normal focal mechanism (ISIDE Working Group, 2016).

Analytical and numerical inversions of accelerometric, interferometric synthetic aperture radar (InSAR), and Global Positioning System data suggested possible interpretations for the fault geometry and the coseismic slip for the 24 August, 26 October, and 30 October events. These events have been interpreted as belonging to the SW dipping normal fault system associated with the Laga-Mount Vettore-Mount Bove alignment (LFS and VBFS in Figure 1a; Cheloni et al., 2017; Huang et al., 2017; Lavecchia et al., 2016; Tinti et al., 2016; Tung & Masterlark, 2018). The possible reactivation of a preexisting compressional structure or the effect of gravity on unconsolidated shallow sediments has also been suggested (Albano et al., 2016; Bonini et al., 2016; Cheloni et al., 2017; Pizzi et al., 2017; Scognamiglio et al., 2018).

The 2016 sequence has been investigated with statistical forecasting methods (Marzocchi et al., 2017), Coulomb stress-based approaches (Mildon et al., 2017; Papadopoulos et al., 2017), and 3-D poroelastic modeling (Tung & Masterlark, 2018). These a posteriori works provided valuable hints about the static stress interaction between the 24 August and the 26–30 October events and highlighted that the majority of aftershocks nucleated in volumes characterized by a coseismic depressurization and postseismic fluid influx (Tung & Masterlark, 2018), thereby confirming the involvement of poroelastic stress changes in the nucleation of aftershocks after the 24 August event. However, all of these analyses require detailed information about the aftershock sequence and the seismogenic crustal volumes that are not available at the beginning of a seismic sequence. To overcome this lack of data, we developed a methodology for the rapid evaluation of the coseismic poroelastic stress perturbations and postseismic poroelastic stress changes under the hypothesis that poroelastic stress changes modulate the nucleation of the majority of aftershocks. We attempt to apply such a methodology to the M_w 6.0 earthquake that occurred on 24 August 2016 in central Italy.

In detail, we evaluated poroelastic stresses using a first-order, 2-D finite element model (FEM) and calculated the coseismic and postseismic stress perturbations and excess pore pressure using linear poroelasticity. The fault geometry and dislocation associated with the 24 August event were calibrated with regard to the focal mechanisms and InSAR coseismic ground displacement data. Then, the postseismic fluid flow diffusion was related to the daily aftershock rates. The results show that the proposed methodology confirms the findings of complex a posteriori modelizations and can provide useful insights into the dynamics of earthquake sequences within very short time periods. Thus, the proposed method has potential benefits for the management of earthquake crises.

2. Data and Methods

2.1. InSAR Data Processing and Results

To simulate the Amatrice earthquake, we constrained the fault slip according to the coseismic ground displacements detected by ascending and descending InSAR data along the satellite line of sight (LoS). The data set (see Table S1 for the details) consists of two pairs of InSAR images acquired on 21 and 27 August by the Sentinel 1-A (S1-A) and B (S1-B) missions of the European Space Agency. The footprints of the S1 data frames are shown in the inset in Figure 1a.

With respect to previous interferometric analyses (Cheloni et al., 2017; Lavecchia et al., 2016), we used different software and processing parameters to crosscheck the results. We estimated both the ascending and descending interferograms using the GAMMA[®] SAR software package (Wegmuller & Werner, 1997). A 90-m digital elevation model was used to remove the topographic contribution. Then, SAR images were

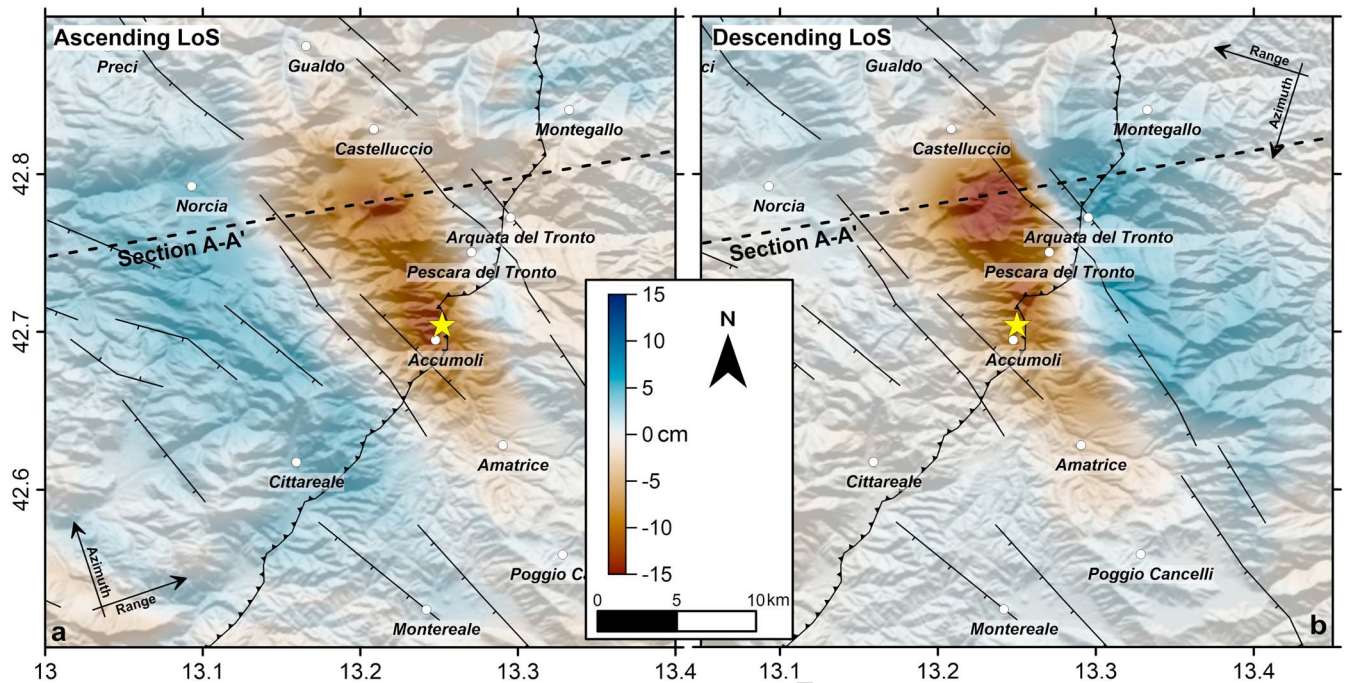


Figure 2. Coseismic ground displacement field associated with the 24 August event from the S1 synthetic aperture radar data. (a) LoS displacements along the ascending track. (b) LoS displacements along the descending track. The black dotted line represents the trace of the section A-A' in Figure 1a. Main faults are from Pizzi and Galadini (2009). For the legend, see Figure 1. LoS = line of sight.

processed to produce 24-m (range) \times 6-m (azimuth) multilook images; thus, an approximately 90-m \times 90-m pixel resolution was obtained. To suppress the signal noise in the presence of rugged topography, we applied Goldstein filtering (Goldstein & Werner, 1998) to both interferograms with an exponent parameter of 0.7 and window size of 8. Finally, we chose the Minimum Cost Flow algorithm (Costantini, 1998) for unwrapping the interferometric phase and subsequently retrieving the displacement maps. Moreover, we also applied adaptive filtering to recover the coherence in the proximity of the epicentral area.

The coseismic LoS displacement pattern of both the ascending and descending interferograms (Figures 2a and 2b) shows the cumulative ground displacements in the period from 21–27 August and incorporates the contribution of the ground displacement caused by both the (major) M_w 6.0 event and the (minor) M_w 5.3 event (Figure 1a). The results do not differ significantly from those of previous studies (Cheloni et al., 2017; Lavecchia et al., 2016), thus confirming the reliability of the computer code and parameters. The ascending and descending maps (Figures 2a and 2b) show that the ground moved away from the satellite (negative values) over the area encompassing the mainshock among the towns of Amatrice, Accumoli, and Castelluccio. A significant component of the motion corresponds to the subsidence of the hanging wall of the seismogenic fault. The maximum deformation is achieved between the villages of Castelluccio and Pescara del Tronto at approximately 9 km from the epicenter. Most of the detected displacement is caused by coseismic slip, although localized displacement patterns have been attributed to shallow gravitational phenomena (Albano et al., 2016; Huang et al., 2017; Polcari et al., 2017).

2.2. Available Seismic Data

Seismic data consisting of early unreviewed data are obtained from the Italian seismic bulletin (<http://cnt.rm.ingv.it/>). The time-dependent completeness magnitude (M_c) associated with such a data set (Chiaraluce et al., 2017; Figure S1b) varies between 1 and 2 in the time interval between the M_w 6.0 Amatrice and the M_w 5.9 Visso events.

2.3. Applied Methodology

Fluid diffusion after large earthquakes alters crustal stresses and can facilitate subsequent events. This phenomenon has been described by a posteriori complex models that can quantify the stress perturbations and

assess the time required for pore fluids to return to hydrostatic conditions (Albano et al., 2017; Antonioli et al., 2005; Jónsson et al., 2003; Malagnini et al., 2012; Nespoli et al., 2018; Tung & Masterlark, 2018; Tung et al., 2018). The extent of the pore pressure perturbation and the flow recovery time depend on the modeling approach and parameters. Modeling strategies for routine applications have to be able to be run quickly and based on past data. Such a strategy could involve the following steps.

- a. Build a 2-D FEM preliminary poroelastic model based on data from the literature for the modeled geomaterials (i.e., the geometry, state, elastic, and hydraulic parameters). In this initial phase, a 2-D geometry is preferred since it is faster to construct and calibrate than a 3-D model and thus provides useful information in a short period (a few days). Moreover, the model must be able to be incrementally refined in successive steps with the availability of new data in the days or weeks after the first event.
- b. Calculate the spatial extent of the coseismic pore pressure perturbation induced by the mainshock. This step requires the constraining of the geometry and slip amplitude of the fault plane associated with the mainshock rupture. Such information is constrained according to the available data, for example, from moment tensor solutions or from preliminary geometries inferred from waveform data, and then refined with the available geodetic and satellite (InSAR) data. For the Amatrice case study, we constrained the fault slip with the available Sentinel-1 InSAR data.
- c. Perform an initial estimation of the time required to dissipate the pore pressure perturbation (T) assuming a range of hydraulic parameters from literature data.
- d. Calculate the theoretical aftershock decay rate according to the modeled pore pressure decay and compare the results with the continuous aftershock data. Eventually adjust the model parameters, that is, the permeability, to improve the fitting with the observed aftershock daily rate.
- e. Perform a new estimation of the T time according to the updated permeability values.
- f. Repeat the steps from “d” to “e” according to the updated aftershock data to improve the estimate of the T value.

2.4. Poroelastic Model

To construct the first-order 2-D poroelastic model, we exploit the built-in diffusion-structural module of the finite element software package MSC MARC 2016 (MSC Software Corporation, 2016), which allowed us to perform fully coupled poroelastic simulations assuming realistic fault geometries and spatially variable material properties.

The 3-D coupling between fluid flow and medium deformations belongs to the theory of linear poroelasticity (Biot, 1941; Rice & Cleary, 1976 ; Wang, 2000). This theory outlines how the stresses are transferred from the solid skeleton to the pore fluid and vice versa.

The constitutive laws that relate strain, fluid mass content per unit volume, stress, and pore pressure are as follows (Segall, 2005):

$$2G\varepsilon_{ij} = \sigma_{ij} - \frac{\nu}{1+\nu}\sigma_{kk}\delta_{ij} + \frac{(1-2\nu)\alpha}{1+\nu}p\delta_{ij} \quad (1)$$

$$\Delta m = m - m_0 = \frac{(1-2\nu)\alpha\rho_0}{2G(1+\nu)} \cdot \left[\sigma_{kk} + \frac{3}{B}p \right] \quad (2)$$

$$q_i = -\rho_0 \frac{\kappa}{\eta} \left(\frac{\partial p}{\partial x_j} - \rho_0 g \delta_{ij} \right) \quad (3)$$

Equation (1) relates the stress and strain in a poroelastic medium, where ν is the drained Poisson ratio; G is the shear modulus; ε_{ij} and σ_{ij} are the strain and the stress tensor components, respectively; α is the Biot-Willis coefficient; p is the pore pressure; and δ_{ij} is the Kronecker delta.

Equation (2) relates the change in fluid mass per unit volume (Δm) to both the sum of normal stresses (σ_{kk}) and pore pressure changes (p). Here ρ_0 is the fluid density, m is the fluid mass content, m_0 is the fluid mass content for a reference state given by the product of the fluid density ρ_0 and the volume of the pore fluid per unit volume of solid (i.e., the porosity n), and B is the Skempton coefficient.

Equation (3) is the constitutive law governing the pore fluid diffusion, that is, Darcy's law, where q_i is the fluid mass flow rate, κ is the permeability, g is the gravitational acceleration, and η is the fluid dynamic viscosity. Equations (2) and (3) are combined with the mass conservation of the infiltrating pore fluid to obtain the diffusion equation.

The poroelastic formulation implemented in the MARC code assumes that the solid grains constituting the medium are incompressible. Such an assumption will affect the magnitude of pore pressures but not the diffusion process. The Skempton (B) and Biot-Willis (α) coefficients can be written as follows (Rice & Cleary, 1976; Wang, 2000):

$$B \cong \frac{K_f}{nK + K_f} \quad (4)$$

$$\alpha \cong 1 \quad (5)$$

where K and K_f are the bulk moduli of the frame and the pore fluid, respectively.

Given the modeling assumptions, a set of eight parameters are required, that is, the shear modulus G , the drained frame bulk modulus K (or, equivalently, the drained Young modulus E and Poisson's ratio ν), the fluid bulk modulus K_f , the porosity n , the permeability k , and the fluid density ρ_0 and dynamic viscosity η .

2.5. FEM Setup

The crust of the Earth behaves as a biphasic medium that consists of a solid skeleton and voids filled with fluids (Fyfe, 2012). At seismogenic depths, that is, the depth interval in which most seismicity occurs, such fluids are water or water-based. Thus, we adopted a fluid-saturated, biphasic numerical model.

Previous analytical and numerical fault solutions (Cheloni et al., 2017; Lavecchia et al., 2016) have shown that the fault slip vector is nearly orthogonal to the fault strike line, whereas the along-strike component of displacement is negligible (i.e., rake $\approx -90^\circ$). To exploit the symmetry in the movement, the section A-A' (Figures 1a and 1b) is modeled to be parallel to the fault slip vector, that is, orthogonal to the fault strike.

A 2-D plane strain FEM (Figure 3) that extends 140 km horizontally and to a depth of 35 km is implemented. The mesh is composed of eight-node, isoparametric quadrilateral elements (9,094 elements) that vary in size and are coarser with increasing depth. The size ranges from approximately 0.3 km at the upper boundary and on the fault trace to 1 km at the bottom and sides of the model.

The mechanical boundary conditions consist of roller support at the sides, while the bottom is fixed along both the horizontal and vertical directions. Regarding the hydraulic boundary conditions, the upper edge (i.e., at zero depth) features atmospheric pressure constraints, and the lower edge is assumed to be impermeable. The hydrostatic pore pressure condition was assigned to the model sides to simulate a flowing boundary.

The tectonic setting of the study area is primarily characterized by NW-SE trending and SW dipping principal thrust planes within the arcuate shape of the central Apennines fold-and-thrust belt (Calamita et al., 2000; Lavecchia et al., 1994) and by NW-SE trending high-angle normal faults (Figures 1a and 1b), with the former generated during the compressional tectonic phase responsible for the construction of the mountain chain in the Neogene and the latter generated in the Quaternary and related to the ensuing extensional tectonic regime that is still currently active. The thrust sheets are composed of a Meso-Cenozoic pelagic carbonate succession that grades upward into Neogene synorogenic siliciclastic deposits (Pizzi et al., 2002; Pizzi & Galadini, 2009).

This complex geology is discretized into three horizontal strata with no faults except for the causative fault of the 24 August event (Figure 3). Each layer presents different elastic and hydraulic properties. The upper and middle layers correspond to the pelagic carbonate succession while the lower layer corresponds to the crystalline basement (see numbers 2 and 3 in Figure 1b). From top to bottom, the three layers are 4, 6, and 25 km thick (Scisciani et al., 2014). The continental and foredeep terrigenous deposits (number 1 in Figure 1b) have not been modeled since we are interested mainly in the poroelastic stress changes at seismogenic depths (i.e.,

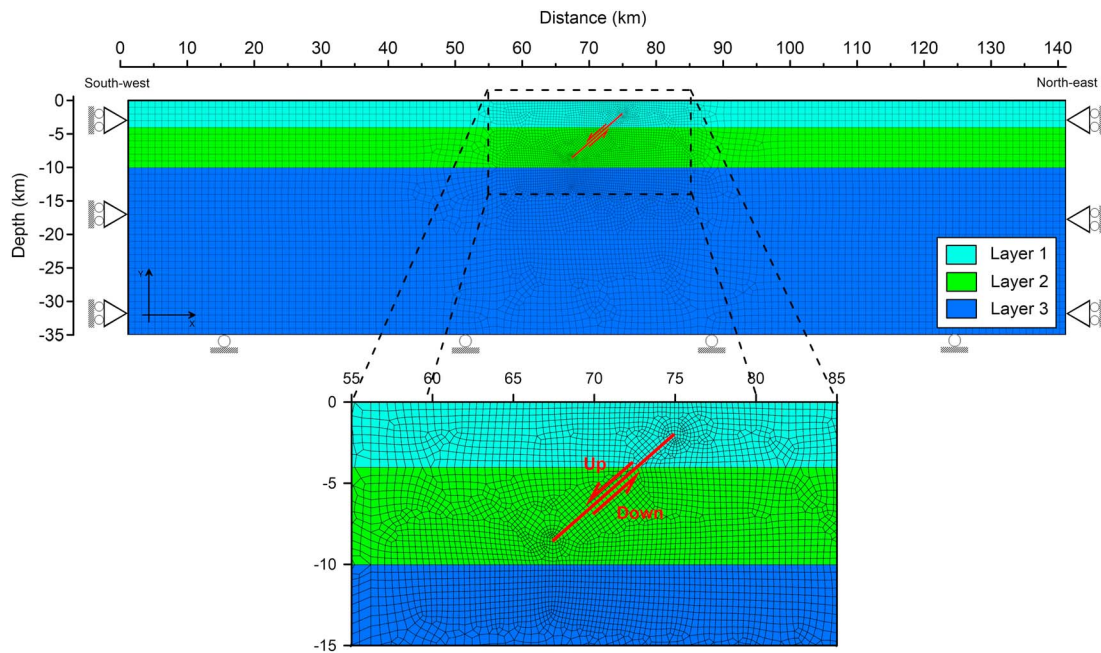


Figure 3. Simplified finite element model of the geological cross section A–A' of Figure 1b. The model grid extends 140 km horizontally and to a depth of 35 km. The red line represents the 24 August 2016 causative fault according to Cheloni et al. (2017). The upper (Up) and lower (Down) red arrows represent the applied edge loads used to simulate the coseismic slip. The three horizontal layers (related parameters are reported in Table 1) schematize the geological units shown in Figure 1b: layers 1 and 2 = pelagic siliciclastic and carbonate successions and layer 3 = crystalline basement, topped by anhydrite and dolomite deposits.

>4 km). Such an approximation of the complex geometry of the investigated area (Figure 1b) has been considered acceptable since we are examining the first-order, large-scale effects of poroelastic stress changes caused by fault slip.

The causative fault of the 24 August mainshock is modeled in accordance with the fault geometry retrieved from moment tensor solutions (ISIDe Working Group, 2016) and the inversion of Global Positioning System and InSAR coseismic data (Cheloni et al., 2017). The fault is modeled using a contact interface dipping approximately 40° and extending approximately 10 km (red segment in Figure 3). Nodes are doubled at the interface; thus, the upper and lower parts of the domain can move relative to each other. The contact interface is assumed to be impermeable; therefore, fluid cannot flow across it. Although fault planes are usually considered porous surfaces, observations and experimental data show that, as slip increases, faults develop a thick, impermeable gouge layer (Parsons et al., 1999; Scholz, 1987). Consequently, the modeled fault is interpreted as mostly behaving as a barrier to fluid flow directed orthogonally to the fault plane (Albano et al., 2017; Piombo et al., 2005).

The fault slip is simulated by applying edge loads to the top and bottom edges of the fault (up and down arrows in Figure 3). These loads are parallel but have different magnitudes and opposite directions.

The elastic and hydraulic properties of geomaterials are known to depend on rheological anisotropies, the joint density and orientation, and previous stress paths (Carminati et al., 2010). However, the model parameters also depend on the size of the domain. In our kilometer-scale model, an equivalent continuum approach is adopted (Sitharam et al., 2001). In particular, each stratum is assumed to be continuous and isotropic, and we derive the equivalent parameters from the geomechanical properties of both the intact rock and joints.

The elastic constants are derived from field and literature data. In detail, the drained Poisson's ratios are selected according to data from the literature (Finocchio et al., 2013; Peltzer et al., 1998; Vadacca et al., 2016). The stiffness values for layers 1 to 3 are constrained according to an up-to-date seismic velocity model of the study area (Carannante et al., 2013). The retrieved dynamic Young's moduli (Table 1) are converted to static Young's moduli according to the empirical relationship proposed by Brotons et al. (2016; equation (6)):

Table 1
Elastic, Hydraulic, and State Parameters Adopted in the Numerical Analysis

Material property	Parameter	Layers		
		1	2	3
Mass density ^a	ρ (kg/m ³)	2,500	2,600	2,700
Drained Poisson's ratio ^a	ν	0.26	0.25	0.23
Drained dynamic Young modulus ^b	E_{dyn} (Pa)	5.94×10^{10}	7.38×10^{10}	9.34×10^{10}
Drained static Young modulus ^c	E_{st} (Pa)	5.34×10^{10}	6.89×10^{10}	9.1×10^{10}
Fluid bulk modulus	K_f (Pa)	2.2×10^{10}		
Fluid dynamic viscosity	η (Pa/s)	0.001		
Fluid density	ρ_0 (kg/m ³)	1000		
Skempton coefficient ^d	B	0.54	0.49	0.44
Porosity ^e	n	0.05	0.05	0.05
Permeability ^f (Kuang & Jiao, 2014)	k_s (m ²)	1×10^{-12}		
	α	0.25		
	k_r (m ²)	1×10^{-14}	1×10^{-15}	1×10^{-16}
		1×10^{-17}		

^aValues from Finocchio et al. (2013) and Vadacca et al. (2016). ^bValues from Carannante et al. (2013). ^cStatic Young's moduli are calculated according to equation (6) as a function of the dynamic Young's moduli (E_{dyn}) and the rock mass density (ρ). ^dValues computed from equation (4). ^eValues from Agosta et al. (2007). ^fPermeability parameters of equation (7) (Kuang & Jiao, 2014). k_s = surface permeability, k_r = permeability at high depth, and α = dimensionless decay index. Values from Agosta et al. (2007), Gleeson et al. (2014), and Kuang and Jiao (2014).

$$E_{\text{st}} (\text{GPa}) = 11.531 \cdot \rho^{-0.457} (\text{kg/m}^3) \cdot E_{\text{dyn}}^{1.251} (\text{GPa}) \quad (6)$$

where ρ (kg/m³) is the mass density, E_{st} is the static Young's modulus, and E_{dyn} is the dynamic Young's modulus, both in gigapascals. The derived static Young's moduli (Table 1) are similar to those retrieved by other studies (Mirabella et al., 2008) and adopted by other numerical models (Finocchio et al., 2016, 2013; Vadacca et al., 2016) for the same area.

Regarding the hydraulic parameters, data from the literature indicate considerable variability. The experimental data show that the shallow permeability and porosity range from 10^{-18} to 10^{-12} m² and from 1–10%, respectively (Agosta et al., 2007). Moreover, the permeability of the Earth's crust decreases with depth (Gleeson & Ingebritsen, 2012). Thus, a parametric analysis is performed based on different permeability profiles according to equation (7) (Kuang & Jiao, 2014):

$$\log k = \log k_r + (\log k_s - \log k_r) \cdot (1 + z)^{-\alpha} \quad (7)$$

where z is the depth, k_s (m²) is the surface permeability, k_r (m²) is the permeability at greater depth, and α (dimensionless) is a decay index.

In the above equation, the surface permeability (k_s) is fixed at the mean value retrieved for the study area from the literature data (Agosta et al., 2007; Gleeson, 2014; Gleeson et al., 2014). The decay index (α) is fixed to the typical value adopted for the upper crust (Kuang & Jiao, 2014), while the permeability at greater depth (k_r) is varied parametrically among the values reported in Table 1. The permeability profiles given by equation (7) and the discretization adopted in the numerical model are shown in Figure S2. The porosity is held constant for layers 1 to 3 (Table 1).

The coupling among the solid and fluid phases is simulated through three steps. In the first step (the interseismic phase), the initial stress and pore pressure distributions are established by applying a gravitational load. The pore pressure distribution at the end of this phase increases linearly with depth.

In the second step (the coseismic phase), the model fault is allowed to slip instantaneously by imposing two nonuniform edge loads on the upper and lower faces of the fault (Figure 3), thus simulating the 24 August event. No friction is assumed at the contact interface.

In the third step (the postseismic phase), no further loads are applied. During this phase, the evolution of the fluid pore pressures and stress changes caused by the coseismic Δp relaxation are calculated for approximately 2 months, thus simulating the period of time between the 24 August mainshock and the 26–30

October events. In this phase, the modeled fault plane is allowed to slip assuming a frictionless contact interface.

2.6. Pore Pressures and Aftershock Decay Rate

The role of poroelastic fluid flow in triggering aftershocks is investigated according to the Nur and Booker (1972) hypothesis. These authors solved the problem of aftershock daily rates caused by pore fluid fluxes induced by a large dislocation occurring in a porous medium, and they postulated that the number of aftershocks in a volume near the mainshock should be proportional to the rate of change of the pore pressure integrated over the region where the pore pressures are changing after the earthquake (equation (8)):

$$\frac{dN}{dt} = \frac{1}{c} \cdot \int_{\Omega} \left(\frac{\delta P}{\delta t} \right) dv \quad (8)$$

where dN/dt is the aftershock decay rate, Ω is the integration domain, $\partial P/\partial t$ is the temporal derivative of pore fluid pressure, and c is a normalization constant with the physical dimensions of pressure times volume. Equation (8) defines a curve representing the theoretical aftershock decay rate following the pore fluid diffusion. Such a curve can be computed from the pore pressures simulated by FEM by rewriting equation (8) as follows (Bosl & Nur, 2002):

$$\frac{dN}{dt} \approx \frac{1}{c} \cdot \sum_{i=1}^M \frac{p(t_n) - p(t_{n-1})}{\Delta t} v_i \quad (9)$$

where M is the total number of selected grid nodes in the FEM model; $p(t_n)$ and $p(t_{n-1})$ are the simulated nodal pore pressures at the current (n) and previous ($n-1$) time, respectively; Δt is the time step adopted in the FEM analysis; and v_i is the volume associated with the i th node.

The parameter c is empirically determined by finding the value that minimizes the mean absolute error (MAE; equation (10)) between the theoretical aftershock decay curve from equation (9) and the observed aftershock daily rate.

$$\text{MAE} = \frac{1}{n} \sum_{i=1}^n |x_p - x_o| \quad (10)$$

where x_p and x_o are the predicted and observed values, respectively, and n is the number of observations.

2.7. Coulomb Stress Changes

As a benchmark of the reliability of the results obtained with the simplified 2-D poroelastic model, we estimated the change in the Coulomb stress (ΔCFS) after the coseismic slip and during the whole postseismic phase, and we compared the observed changes with the spatial distribution of the aftershocks along the cross section A-A' of Figure 1a. The ΔCFS is calculated as follows (Cocco & Rice, 2002):

$$\Delta\text{CFS} = \Delta\tau + \mu \cdot (\Delta\sigma_n + \Delta p) = \Delta\tau + \mu \cdot \Delta\sigma'_n \quad (11)$$

where $\Delta\tau$ is the shear stress change (computed along the slip direction), μ is the static friction coefficient (Harris, 1998; King et al., 1995), $\Delta\sigma_n$ is the fault-normal total stress change, Δp is the pore pressure change, and $\Delta\sigma'_n$ is the effective fault-normal stress change. Because the numerical model adopts a positive sign convention for tension and a negative sign convention for compression, a positive ΔCFS indicates normal fault weakening. The static fault friction coefficient ranges between 0.6 and 0.8 for most rocks (Harris, 1998). Because crustal rocks are fractured, a lower bound for the friction coefficient is assumed ($\mu = 0.6$; Piombo et al., 2005).

3. Results

The results of the numerical analyses are expressed in terms of displacements and pore pressures exceeding the hydrostatic values. Both positive and negative pore pressure changes with respect to the hydrostatic values are hereinafter indicated using Δp , and we use the terms “suprahydrostatic” in the case of a pore pressure increase and “subhydrostatic” in the case of a pore pressure decrease.

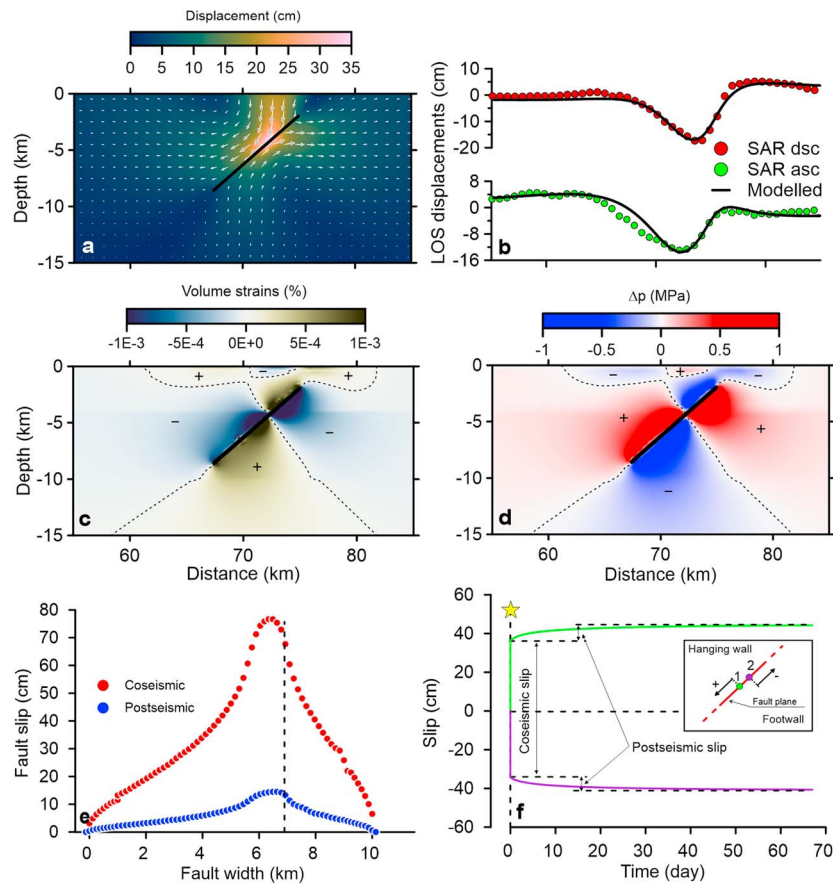


Figure 4. Results of the simulated coseismic phase. (a) Coseismic deformation pattern after the simulated 24 August 2016 event. The arrows represent the displacement field. (b) Comparison between the measured and modeled coseismic ascending and descending LoS displacement profiles along the A–A' section (Figure 1). (c) Coseismic volumetric strains. Positive values indicate volume dilation; negative values indicate compression. (d) Coseismic Δp pattern, showing the pore pressure increase (+) and decrease (–) with respect to the hydrostatic values. (e) Coseismic (red symbols) and cumulative postseismic slip (24 August to 26 October; blue symbols) along the modeled fault width, from the bottom (0 km) to the top (10 km). (f) Computed slip over time at two nodes lying along the modeled fault (for the location, see the dashed black line in e). Points 1 and 2 are located in the hanging wall and the footwall, respectively (see the inset in f). Postseismic slip is computed for the model with $k_r = 1 \times 10^{-15} \text{ m}^2$. SAR = synthetic aperture radar; LoS = line of sight.

3.1. Coseismic Phase

The modeled fault slip produces a deformation pattern (Figure 4a) that involves a volume of the medium **F4** mainly localized at the hanging wall of the dislocated fault. The displacement pattern and vectors with a maximum amplitude of approximately 35 cm indicate slip along the causative fault and are consistent with the solutions proposed by Cheloni et al. (2017) and Lavecchia et al. (2016). The modeled coseismic deformations are projected along the satellite LoS and compared with the InSAR-derived LoS displacements along section A–A' (Figure 4b). The agreement between the modeled and measured LoS displacements is satisfactory (black line versus colored circles in Figure 4b). Additionally, the root-mean-square error (RMSE) is less than 2 cm for both the ascending and descending ground displacements ($\text{RMSE}_{\text{ASC}} = 1.67 \text{ cm}$; $\text{RMSE}_{\text{DSC}} = 1.83 \text{ cm}$), which are less than or equal to the RMSE values obtained by other authors (Cheloni et al., 2017; Lavecchia et al., 2016).

The resulting coseismic slip (Figure 4e) causes shear and volumetric changes in the medium (Figure 4c). Because the model is fluid-saturated, the volumetric changes develop a Δp pattern (Figure 4d). The Δp values reach nearly $\pm 2 \text{ MPa}$ in areas close to the fault zone and extend vertically and laterally for more than 15 km (Figure S3). In particular, suprahydrostatic pore pressures develop in areas affected by volumetric

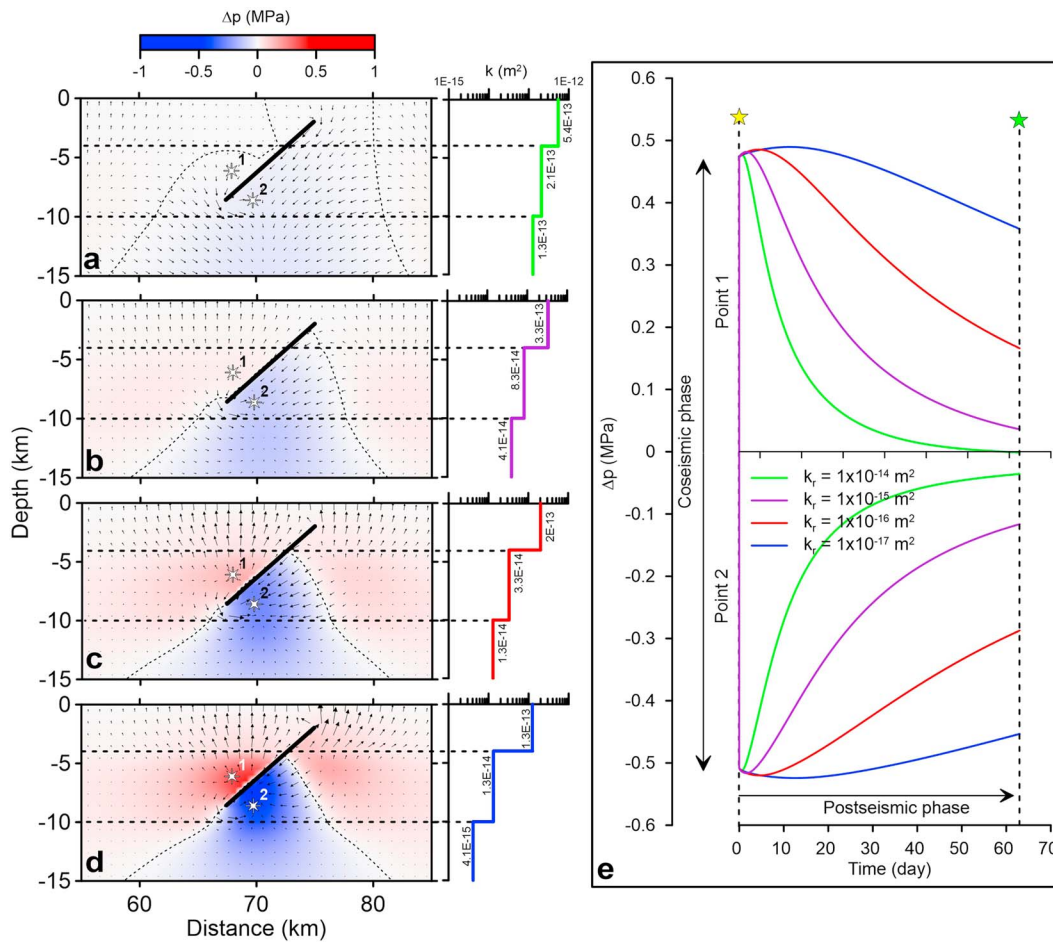


Figure 5. Pore pressure changes (Δp) and decay with respect to the hydrostatic values for different permeability profiles. Panels on the left show the Δp pattern 63 days after the 24 August event (i.e., at the time of the 26 October earthquake) assuming that the permeability profiles (panels in the center) correspond to (a) $k_r = 1 \times 10^{-14}$ m², (b) 1×10^{-15} m², (c) 1×10^{-16} m², and (d) 1×10^{-17} m² (also see Table 1 and Figure S2). (e) The panel on the right shows the coseismic Δp peak and postseismic decay at points 1 and 2 in (a)–(d) (white stars) for different permeability profiles. The yellow and green stars represent the 24 August (M_w 6.0) and 26 October (M_w 5.9) earthquakes, respectively.

compression, whereas subhydrostatic pore pressures develop in areas affected by volumetric dilation. These Δp values are transient and gradually dissipate in the postseismic phase because of fluid diffusion.

3.2. Postseismic Phase

3.2.1. Fluid Diffusion and Pore Pressure Decay

In the postseismic phase, fluids spread from regions with suprahydrostatic pore pressures to regions with subhydrostatic pore pressures, thus gradually restoring the hydrostatic condition.

The fluid flow rate and Δp recovery depend on the assumed permeability magnitude and spatial distribution. Indeed, different permeability magnitudes accelerate or delay the fluid flow and Δp dissipation; that is, lower permeability corresponds to longer times required to reach hydrostatic pore pressures.

For the model with the highest permeability (i.e., $k_r = 1 \times 10^{-14}$ m²), the postseismic Δp values computed at the time of the 26 October event are close to zero (Figure 5a), indicating that hydrostatic pore pressures are almost restored. For lower-permeability values (Figures 5b–5d), pore fluids are still spreading in the medium at the time of the later earthquake. In particular, the postseismic Δp values correspond to approximately 20, 33, and 50% of the coseismic Δp for $k_r = 1 \times 10^{-15}$ m², 1×10^{-16} m², and 1×10^{-17} m², respectively.

Nonuniform permeability allows for different Δp recovery times at different nodes in the domain. In fact, the assigned permeability, which decreases with depth, allows for a faster Δp recovery for points near the surface

than for points located at seismogenic depth (see Figures 5a–5d). Indeed, the time histories of Δp at points 1 and 2 in Figure 5e are not symmetric since point 1 is located at a shallower depth than point 2 and therefore experiences faster fluid flow and Δp recovery than point 2.

The maximum Δp values at points 1 and 2 are reached several days after the coseismic slip (Figure 5e) because the delay time is inversely proportional to the assumed permeability. In fact, the calculated gradients for Δp curves (Figure S4) show a change in the sign at approximately 0.5, 2, 5, and 12 days for $k_r = 1 \times 10^{-14} \text{ m}^2$, $1 \times 10^{-15} \text{ m}^2$, $1 \times 10^{-16} \text{ m}^2$, and $1 \times 10^{-17} \text{ m}^2$, respectively. Since pore pressures and stresses are fully coupled, postseismic fluid diffusion and Δp dissipation allow for further slip (i.e., afterslip) along the mainshock causative fault (Figures 4e and 4f; Albano et al., 2017). If the afterslip rate is faster than the fluid diffusion rate, then a slight Δp increase is produced in the early postseismic phase, which is followed by a gradual decay when the afterslip rate is negligible with respect to the pore fluid diffusion rate (Figures 4f and 5e). Such an effect depends on the adopted medium permeability; that is, a higher permeability corresponds to a smaller effect on the afterslip and pore fluids (Figure 5e).

3.2.2. Aftershocks and Pore Fluid Diffusion

The adopted permeability profiles produce different Δp rates and then different recovery times T of the hydrostatic pore pressures. Postseismic Δp rates are compared with the observed aftershocks according to the Nur and Booker (1972) hypothesis to select the most plausible permeability and the corresponding recovery time T . The theoretical aftershock daily rate curves have been calculated from the simulated nodal postseismic pore pressures according to equation (9). Regarding the integration domain, we selected all the nodes of the FEM located at a depth between 4 and 10 km and in areas where the pore pressures are increasing in the postseismic phase (Bosl & Nur, 2002). In regions where pore pressures are decreasing, the faults are strengthened and aftershocks will tend to be suppressed. We calculated several theoretical aftershock curves corresponding to the different permeability profiles assumed in the models (Figures 5 and S2). Each curve is scaled with respect to the early estimates of the aftershock daily rate by selecting the coefficient c (equation (9)) that minimizes the MAE function (equation (10)).

A frequently ubiquitous issue associated with aftershock sequences is related to the M_c of the aftershock data and how this parameter affects the comparison with the theoretical aftershock curves. According to the a posteriori estimation of the time-dependent M_c (Chiaraluce et al., 2017; Figure S1b), we plotted the observed aftershock daily rate assuming $M_c \geq 1.5$, $M_c \geq 1.7$, and $M_c \geq 2.0$. First, the theoretical curves are compared with the daily aftershocks in the period 24 August to 26 October 2016, that is, between the M_w 6.0 Amatrice and the M_w 5.9 Visso earthquakes (Figures 6a–6c). The observed aftershock daily rates were then compared with the computed theoretical aftershock decay rates to investigate the effect of choosing a different M_c value on the fit. In all three cases (Figures 6a–6c), the lower MAE belongs to the curve for $k_r = 1 \times 10^{-14} \text{ m}^2$. Curves for $k_r = 1 \times 10^{-16} \text{ m}^2$ and $k_r = 1 \times 10^{-17} \text{ m}^2$ present higher MAE values and are not shown in the figure. Running a new FEM assuming a permeability profile between $k_r = 1 \times 10^{-15} \text{ m}^2$ and $1 \times 10^{-14} \text{ m}^2$ (blue curve in Figures 6a–6c; with $k_r = 3.5 \times 10^{-15} \text{ m}^2$) shows a better fit for $M_c \geq 1.5$, while for $M_c \geq 1.7$ and $M_c \geq 2$, the MAE is slightly higher than for the model with $k_r = 1 \times 10^{-14} \text{ m}^2$. The MAE values for the best fit Omori-Utsu law are close to the estimates obtained with equation (9).

The performance of the fit is further investigated by comparing the theoretical and observed aftershock daily rates at intermediate times, for example, at 6, 12, 18, 24, 30, 36, 42, 48, 54, and 60 days from the mainshock. In all cases (Figures 6d–6f), lower MAE values always belong to the curves with $k_r = 3.5 \times 10^{-15} \text{ m}^2$ and $k_r = 1 \times 10^{-14} \text{ m}^2$ for $M_c \geq 1.5$, 1.7, and 2. Therefore, a reliable selection of the permeability profile that is consistent with the ongoing aftershocks is possible only one week after the 24 August event.

Once the permeability profiles compatible with the observed aftershock daily rates have been identified, the modeled postseismic phase is extended to one year after the 24 August event to estimate the recovery time of hydrostatic pore pressure T at seismogenic depth. In particular, the fluid diffusion is assumed to be concluded when the Δp gradient reaches a value of approximately 0.5 kPa/day. A shift of approximately 20 days is observed among the curves showing lower MAE values (Figure 7), with a value of approximately $T = 60$ days for $k_r = 1 \times 10^{-14} \text{ m}^2$ and $T = 80$ days for $k_r = 3.5 \times 10^{-15} \text{ m}^2$.

3.2.3. Aftershocks and Coulomb Stress

The effectiveness of the performed poroelastic analysis has been evaluated by calculating the ΔCFS in the coseismic and postseismic phases according to equation (11) and comparing these results with the

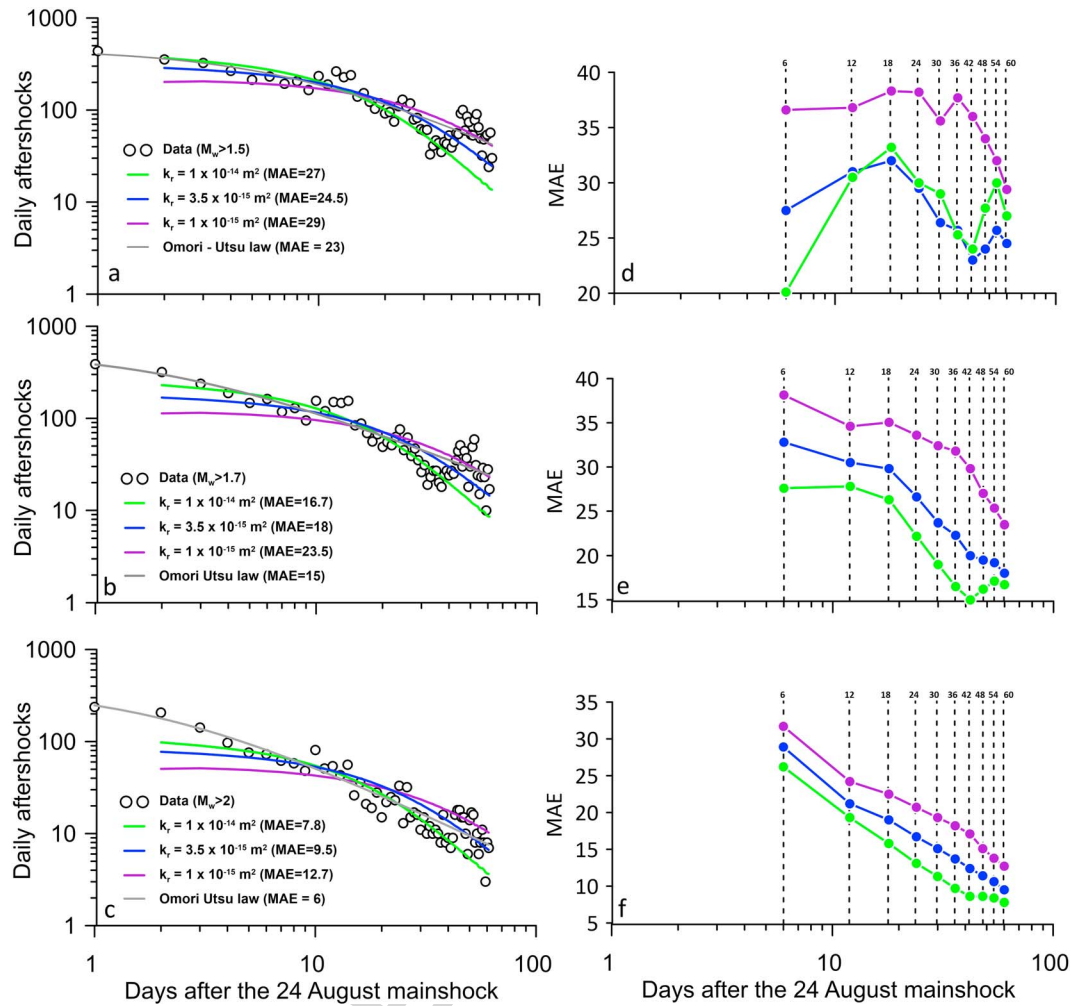


Figure 6. Comparison between the theoretical and observed aftershock daily rate in the period 24 August to 26 October 2016 assuming (a) $M_c \geq 1.5$, (b) $M_c \geq 1.7$, and (c) $M_c \geq 2$. The gray line represents the best fit Omori-Utsu law for the experimental data. MAE calculations at 6, 12, 18, 24, 30, 36, 42, 48, 54, and 60 days from the mainshock assuming (d) $M_c \geq 1.5$, (e) $M_c \geq 1.7$, and (f) $M_c \geq 2$. MAE = mean absolute error.

aftershock distribution at depth. In particular, we sought to identify where the ΔCFS increases in the postseismic phase because of fluid flow in the crust (Albano et al., 2017; Piombo et al., 2005).

The Coulomb stresses are calculated on both normal fault planes dipping 40° southeast and conjugate planes dipping 50° northwest according to the mean focal mechanisms of the aftershock sequence (Chiaraluce et al., 2017).

The results for the model with $k_r = 3.5 \times 10^{-15} \text{ m}^2$ are shown in Figure 8. In particular, in the coseismic phase, the fault slip produces the ΔCFS pattern in Figure 8a. The computed ΔCFS caused by elastic fault dislocation highlights the volumes that are strengthened (negative ΔCFS) or weakened (positive ΔCFS), thus producing patterns similar to the solutions proposed for the same zone in other studies (Nostro et al., 2005; Serpelloni et al., 2012).

In the postseismic phase, Δp values decrease, leading to a ΔCFS change (equation (11)). The regions with suprahydrostatic coseismic Δp values experience a ΔCFS decrease, whereas regions with subhydrostatic coseismic Δp values experience a ΔCFS increase. The obtained ΔCFS values due to only poroelastic relaxation (Figure 8b) are statistically significant compared with the coseismic values, reaching approximately ± 2 MPa in regions close to the fault trace. Therefore, the ΔCFS pattern 63 days after the 24 August event (given by the algebraic sum of ΔCFS in Figures 8a and 8b; Figure 8c) is different from the coseismic pattern. Notably, following the postseismic Δp dissipation, certain volumes where the coseismic ΔCFS was positive

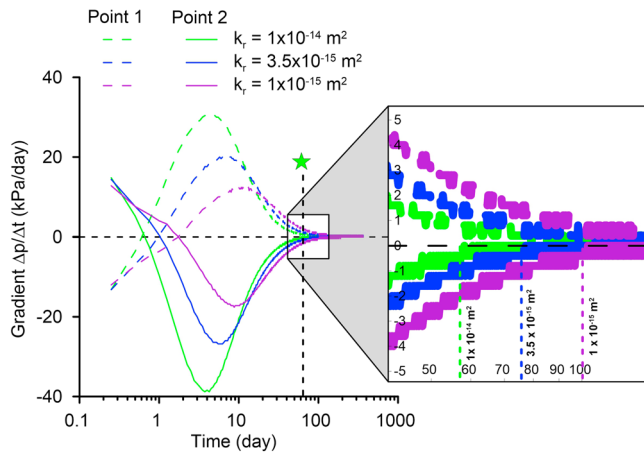


Figure 7. Calculated gradient for Δp curves at points 1 and 2 located in Figure 5 for the permeability values reported in Figure 6. The postseismic phase has been extended to one year after the 24 August event to investigate the recovery time of hydrostatic pore pressure (T). The fluid diffusion is assumed to be concluded when the gradient reaches a value of approximately 0.5 kPa/day. The green star represents the 26 October (M_w 5.9) earthquake.

(i.e., facilitating earthquakes) now show negative ΔCFS value (i.e., inhibiting earthquakes). In contrast, volumes where the coseismic ΔCFS was negative (i.e., inhibiting earthquakes) now show positive ΔCFS values (i.e., facilitating earthquakes). In detail, we identified four regions characterized by different behaviors (Figure 8c): (1) regions where the coseismic ΔCFS is positive and increases further in the postseismic period (ΔCFS_{c+} , ΔCFS_{p+}); (2) regions where the coseismic ΔCFS is positive but decreases in the postseismic period (ΔCFS_{c+} , ΔCFS_{p-}); (3) regions where the coseismic ΔCFS is negative but increases in the postseismic period (ΔCFS_{c-} , ΔCFS_{p+}); and (4) regions where the coseismic ΔCFS is negative and decreases further in the postseismic period (ΔCFS_{c-} , ΔCFS_{p-}).

The described ΔCFS evolution is shown at several points, close the fault trace (Figures 8c and 8d). At point 1 (Figure 8d), the positive coseismic ΔCFS increases further in the postseismic phase because the Δp values increase from subhydrostatic to hydrostatic values. At point 2, the positive coseismic ΔCFS decreases in the postseismic phase because the volume is gradually strengthened by the Δp decrease from suprahydrostatic to hydrostatic values. At point 3, the negative coseismic ΔCFS gradually increases in the postseismic phase because the subhydrostatic Δp values increase to positive values. Finally, at point 4, the negative coseismic

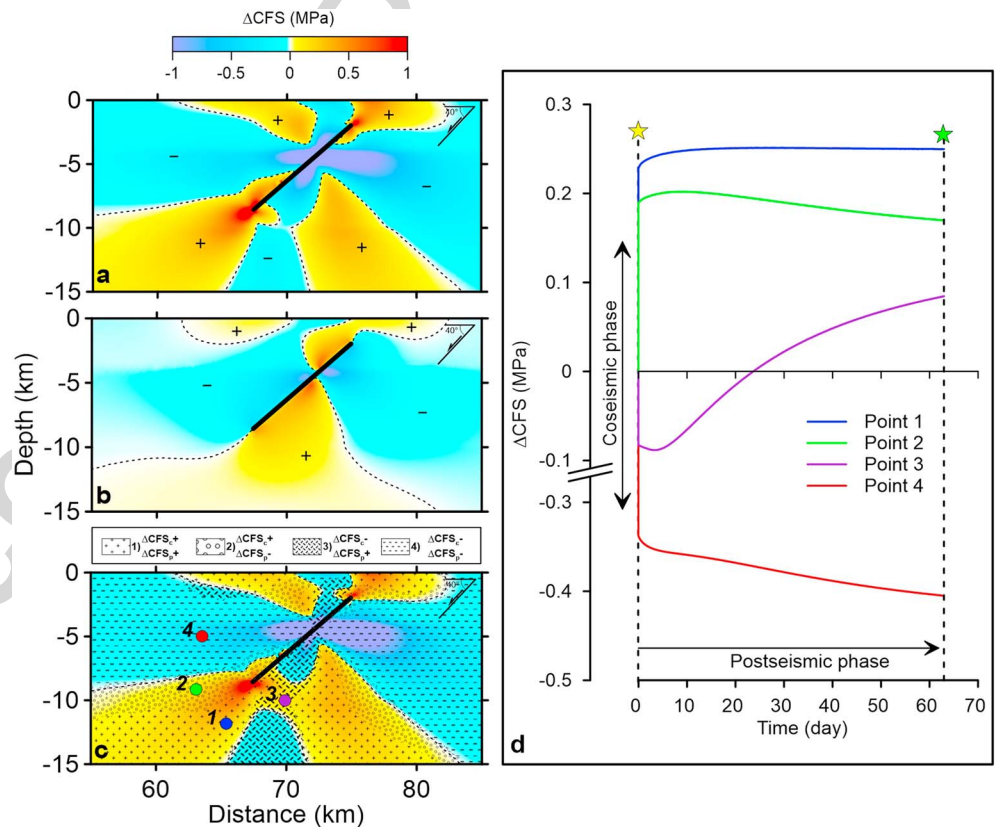


Figure 8. Model of stress changes (ΔCFS) and evolution over time (see Figure 3 for the location of the model). The dip angle and plunge of the target faults are indicated in the top right corner. However, the target faults are not represented in the figure to avoid cluttering. (a) Coseismic ΔCFS pattern on 24 August 2016. (b) Postseismic ΔCFS induced by pore fluid diffusion 63 days after the 24 August event. (c) Coseismic plus postseismic ΔCFS model (i.e., the sum of a and b). The dashed lines in (a)–(c) indicate the null ΔCFS . (d) Evolution over time of ΔCFS for points 1–4 located in (c). The yellow and green stars represent the 24 August (M_w 6.0) and 26 October (M_w 5.9) earthquakes, respectively.

Δ CFS values decrease further in the postseismic phase. Similar results but with a different pattern are obtained for conjugate normal planes (Figure S5).

Aftershocks are expected to occur preferentially in regions characterized by positive Δ CFS in the postseismic phase. Hence, a spatial analysis is conducted by superimposing the aftershocks within a distance of 5 km from the modeled section on the postseismic Δ CFS, which was calculated for the principal and conjugate planes at 5, 10, 20, 40, and 63 days after the mainshock. We then calculated the percentage of aftershocks that originated in positive Δ CFS volumes for at least one of the two assumed fault planes for each of the selected time intervals. The aftershocks appear evenly distributed in both the positive and negative Δ CFS volumes over time (Figure 9a). However, a spatial correlation is found between the Δ CFS and aftershocks since the percentage of aftershocks in positive Δ CFS volumes starts to increase slightly after 10 days from the mainshock (Figure 9b) and reaches approximately 63% of the total aftershocks at 63 days after the 24 August event at the expense of aftershocks in negative Δ CFS volumes. Neglecting the poroelastic changes in the Δ CFS pattern results in a lower percentage of aftershocks falling on positive coseismic Δ CFS volumes. Indeed, the comparison between the coseismic Δ CFS pattern (Figure 9a for $t = 0$) and the aftershocks at 63 days after the 24 August event shows that a lower percentage of aftershocks falls in positive Δ CFS volumes (red and blue rings in Figure 9b) compared with the postseismic Δ CFS pattern, that is, approximately 53%.

4. Discussion

Our results indicate that for the adopted simplified modeling approach and the assumed permeability profiles, transient fluid pore pressures are predicted at seismogenic depths during the investigated period (i.e., 24 August to 26 October 2016; Figure 5). The numerical results indicate that the coseismic pore pressure perturbation caused by a M_w 6 earthquake is greater than ± 1 MPa (Figure 4d) and becomes negligible at distances of approximately 10 km, that is, greater than the fault dimensions (Figure S3). The time required to dissipate the Δp perturbation is inversely proportional to the permeability because lower permeability causes a slower dissipation of pore pressures. A comparison between the observed aftershock daily rate and the rate predicted with the simulated pore fluid diffusion (Figure 6) was performed to identify the permeability profiles that are compatible with the observations and then estimate the time interval T required to dissipate pore pressures at seismogenic depths (i.e., from $T = 60$ to $T = 80$ days). The estimated time is compatible with the nucleation of the 26 October M_w 5.9 Visso earthquake.

The results show that the afterslip occurred in the early postseismic phase due to the initiation of pore fluid diffusion. In turn, the afterslip in turn further increased the pore pressures. This nonlinear behavior is significant only for short times after the mainshock (Figures 4f, 5e, and S4); therefore, at small distances from the fault, the diffusion process and confining stresses prevail at greater spatiotemporal scales. Thus, the choice of the model parameters may be crucial for near-fault issues but can be more relaxed for regional-scale models. However, the computed postseismic slip magnitude could be overestimated since it depends on the adopted residual friction at the contact interface (Albano et al., 2017).

Finally, the Δ CFS identifies where the crust is strengthened or weakened by pore fluid diffusion in the postseismic phase. In particular, postseismic pore pressure transients modify the Coulomb stresses on faults in an area of several square kilometers (Figure 8). The Δ CFS caused by pore fluid diffusion is statistically significant (more than ± 1 MPa; Figure 8b) and could contribute to the generation of aftershocks with magnitudes comparable to that of the mainshock. Therefore, the 26 October (M_w 5.9) event could have been facilitated by the 24 August (M_w 6.0) earthquake and subsequent pore fluid diffusion.

The discrete agreement between the observed aftershock daily rate and the rate predicted by pore fluid diffusion denotes that the majority of aftershocks behave like a diffusive process. In our case, the aftershock pattern is sufficiently described in terms of its temporal evolution but poorly characterized in terms of its spatial pattern.

In terms of the temporal evolution, the choice of the model permeability depends on an aftershock data set that is inherently incomplete (Figures 6 and S1). Indeed, in our case, the best fit permeability k_r varies from 3.5 to 10×10^{-15} m² assuming that our data set has a M_c of 1.5 to 2.0. At depths between 4 and 10 km, the uncertainty in the permeability is approximately 15%. Consequently, such an incomplete data set yields

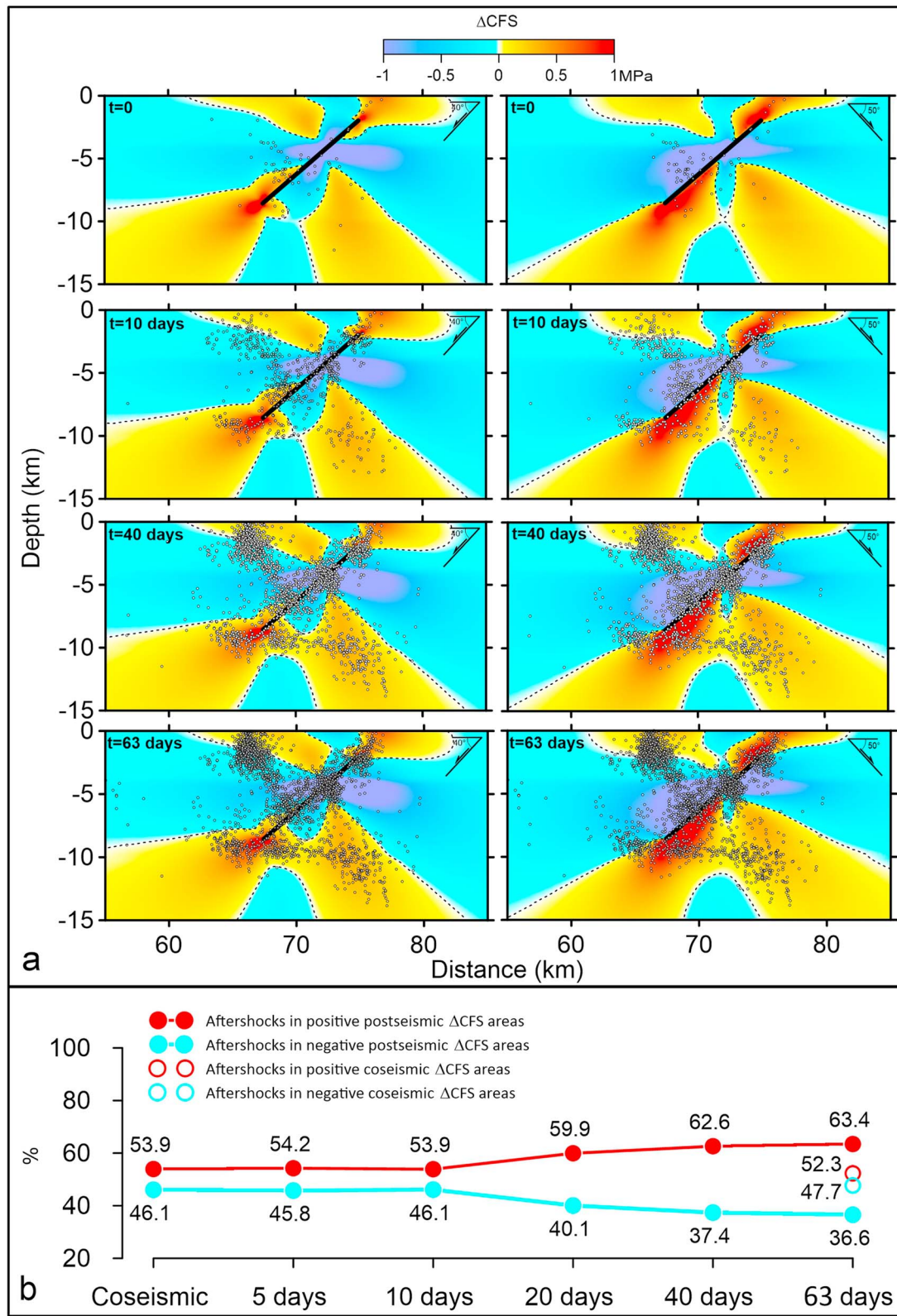


Figure 9. Aftershocks falling in regions with positive and negative ΔCFS . (a) Comparison between the ΔCFS and aftershock locations at $t = 0, 10, 40,$ and 63 days after the 24 August event. (b) Percentage of aftershocks occurring in areas with increasing (red line) or decreasing (blue line) postseismic ΔCFS for normal planes dipping SW or conjugate planes dipping NE calculated at 0, 5, 10, 20, 40, and 63 days after the mainshock.

an uncertainty of 25% for the estimated time required to dissipate pore pressure (approximately 20 days; Figure 7). A possible solution regarding the selection of plausible M_c values could be calculating a priori M_c values for the Italian territory based on the performance of the available seismic network and the available past seismic data (Marchetti et al., 2006). Such an approach could, in principle, improve the efficiency of the seismic network in cases of strong earthquakes.

In terms of the spatial pattern, the ΔCFS pattern is poorly correlated with the relocated aftershocks (Figure 9). Indeed, immediately after the coseismic phase, almost half of the aftershocks fall in areas where the ΔCFS values are negative. However, aftershocks in positive ΔCFS areas slightly increase over time at the expense of aftershocks in negative ΔCFS areas (Figure 9b), reaching approximately 63% of the cumulative aftershocks immediately prior to the 26 October event. Such a percentage is higher than that obtained under the coseismic ΔCFS only assumption (approximately 52%). Therefore, we believe that our modeling approach is acceptable, even if all aftershocks cannot be explained with a diffusion-like mechanism.

Moreover, our modeling approach presents geometric model approximations and unmodeled features. The geometric approximation refers to the plane strain hypothesis and the assumption of a normal-fault dip of 40° . Hence, the anomalous aftershocks could be explained by a more complex fault pattern than the single plane used in this study, that is, a model that includes antithetic or additional synthetic fault planes, and a 3-D slip distribution. Moreover, the Δp pattern is calculated based only on the 24 August event since the largest aftershocks are not included in our calculations of the pore pressures and stress field. Therefore, the resulting coseismic Δp pattern could be more complex. Unmodeled features potentially include the presence of heterogeneities in the elastic and hydraulic material properties as well as the presence of fluid-pressurized regions that can affect the fluid diffusion when these regions are broken after the fault slip (Miller et al., 2004). Such heterogeneities could significantly affect the fluid flow and, consequently, the ΔCFS pattern at depth. More accurate simulations that account for material heterogeneity, different rupture mechanisms, and the aftershock dependency on pore pressure are usually preferred. For instance, a 3-D model could produce more accurate results (Hughes et al., 2010; Nostro et al., 2005; Tung et al., 2018). Indeed, the spatial pattern of the ΔCFS predicted by Tung and Masterlark (2018), who use a 3-D slip model, is generally consistent with the aftershock spatial distribution and explains approximately 80% of the nucleated aftershocks. However, a fully coupled poroelastic 3-D modeling approach requires detailed information on the fault geometry, the amplitude and spatial distribution of the fault slip, and the geometrical and rheological anisotropies of the modeled geomaterials. Moreover, because permeability controls the direction and rate of fluid diffusion in porous media, more accurate knowledge of the permeability structure in and around fault zones are needed to better predict the rate and amplitude of poroelastic stress changes due to pore fluid flow.

Although our numerical model may not currently allow for a detailed description of the postseismic fluid diffusion, the first-order results are robust. In fact, the near-field pore pressures (i.e., at distances comparable to the fault size) are well modeled because of the reasonable fit between the predicted and observed aftershock daily rates. Additionally, the modeled far-field coseismic pore pressures seem to be reasonable. At distances of approximately 100 km, our model estimates pore pressures of approximately 10–20 Pa. Such pressures are compatible with water table oscillations in wells (approximately 20–80 cm), observed after the mainshock by Barberio et al. (2017).

Our estimates are consistent with the findings of a posteriori models. Indeed, Tung and Masterlark (2018) and Walters et al. (2018) identified a strong poroelastic effect with the 26 October event.

Our permeability estimates are consistent with the seismogenic permeability range suggested by Talwani et al. (2007) but lower than those of Townend and Zoback (2000). Such a discrepancy is easily explained by considering that in situ crustal permeability is extremely heterogeneous since it can range over several orders of magnitude (Townend & Zoback, 2000). Therefore, assessing the feasibility of the adopted parameters in heterogeneous materials is somewhat idealistic. Moreover, our permeability estimates are different from the a posteriori point-source approximation model (Walters et al., 2018) and a 3-D numerical model (Tung & Masterlark, 2018) applied in the same area. Such a discrepancy is related to the modeling approach because our model permits only two-dimensional pressure gradients while 3-D models cause a more rapid decay in both the pore pressure field and the number of aftershocks. Moreover, the discrepancy is associated with the assumed permeability, which is uniform in Walters et al. (2018) and Tung and Masterlark (2018).

and variable with depth in our model. Finally, the pore pressure dissipation times (and hence the selected permeability) of Tung and Masterlark (2018) depend on their decision to maximize the Coulomb stresses at the 26 October (M_w 5.9) earthquake location and time, which can only be performed a posteriori.

Although different permeability estimates were obtained, all the modeling approaches generated the same conclusions; thus, the results of these previous studies were consistent with ours.

From a practical perspective, the advantage of the proposed approach is that it is possible to provide a first-order indication of the extent of coseismic pore pressure perturbations (Figure S3) and the postseismic pore pressure decay time T (Figures 6 and 7) at just 1 week after the mainshock (Figures 6d–6f). Therefore, developing this type of analysis and making it more reliable could contribute to better management of seismic emergencies in the future. In fact, multiple large earthquakes are common during seismic sequences and often cause additional casualties (Govoni et al., 2014; Valoroso et al., 2013).

As for civil protection, information such as the duration time of poroelastic stress changes and the spatial extension of the perturbation can provide an initial estimate of the area and time that could be affected by the aftershock sequence. This information can be used to plan the deployment of Red Cross personnel and fuel reserves, investigate infrastructure vulnerabilities, and possibly plan to reduce the vulnerability of critical infrastructure (including roads prone to landslides in mountain areas).

Such an approach could be improved by adding further details about the mechanics underlying faulting, such as the spatiotemporal seismicity model based on the rate-and-state dependent frictional response of fault populations introduced by Dieterich (1994), and it could be implemented via the brick-by-brick approach (Jordan, 2006) commonly used in operational forecasting methods (Marzocchi et al., 2017) to develop a physics-based forecasting approach. Thus, this work contributes to the development of more reliable aftershock forecast models that could be useful in the management of seismic crises and generate additional information for affected populations.

5. Conclusions

In this work, the evolution of a seismic sequence in central Italy was investigated in the framework of poroelasticity theory. For this purpose, a 2-D FEM poroelastic model was developed and calibrated using geological, hydrogeological, satellite, and aftershock data.

Diffusive processes drive the occurrence of aftershocks. In fact, our model showed a good match between the predicted and observed daily earthquake rates. The assumed permeability value at seismogenic depths is the most crucial parameter in determining the aftershock rate.

The 26 October 2016 earthquake occurred when the fluid overpressure had not yet dissipated; thus, the overpressure conditions potentially facilitated the nucleation of subsequent large earthquakes at distances comparable to the fault size. In fact, the numerical analyses indicate that the 24 August event significantly altered the pore pressures to distances of up to approximately 15 km.

This work highlights the need to adequately account for time-dependent poroelastic effects when modeling postseismic and interseismic scenarios. Such an approach can provide insights toward the development of more reliable predictions of earthquake sequences after strong earthquakes.

Acknowledgments

We thank the European Space Agency for providing the S1 data. The data used in this study can be found in the references, tables, and supporting information. Perceptually uniform color maps are used in certain figures (Cramer, 2018a, 2018b). This research was supported by the FISR 2016 research project (ID 0865.010). The contents of this paper represent the authors' ideas and do not necessarily correspond to the official opinion and policies of the Italian Department of Civil Protection.

References

- Agosta, F., Prasad, M., & Aydin, A. (2007). Physical properties of carbonate fault rocks, Fucino basin (central Italy): Implications for fault seal in platform carbonates. *Geofluids*, 7(1), 19–32. <https://doi.org/10.1111/j.1468-8123.2006.00158.x>
- Albano, M., Barba, S., Solaro, G., Pepe, A., Bignami, C., Moro, M., et al. (2017). Aftershocks, groundwater changes and postseismic ground displacements related to pore pressure gradients: Insights from the 2012 Emilia-Romagna earthquake. *Journal of Geophysical Research: Solid Earth*, 122, 5622–5638. <https://doi.org/10.1002/2017JB014009>
- Albano, M., Saroli, M., Moro, M., Falucci, E., Gori, S., Stramondo, S., et al. (2016). Minor shallow gravitational component on the Mt. Vettore surface ruptures related to M_w 6, 2016 Amatrice earthquake. *Annals of Geophysics*, 59(Fast Track 5). doi:<https://doi.org/10.4401/ag-7299>
- Ammon, C. J., Kanamori, H., & Lay, T. (2008). A great earthquake doublet and seismic stress transfer cycle in the central Kuril islands. *Nature*, 451(7178), 561–565. <https://doi.org/10.1038/nature06521>
- Antonoli, A., Piccinini, D., Chiaraluce, L., & Cocco, M. (2005). Fluid flow and seismicity pattern: Evidence from the 1997 Umbria-Marche (central Italy) seismic sequence. *Geophysical Research Letters*, 32, L10311. <https://doi.org/10.1029/2004GL022256>

- Barberio, M. D., Barbieri, M., Billi, A., Doglioni, C., & Petitta, M. (2017). Hydrogeochemical changes before and during the 2016 Amatrice-Norcia seismic sequence (central Italy). *Scientific Reports*, (may), 1–12. doi:<https://doi.org/10.1038/s41598-017-11990-8>
- Biot, M. A. (1941). General theory of three-dimensional consolidation. *Journal of Applied Physics*, 12(2), 155–164. <https://doi.org/10.1063/1.1712886>
- Bonini, L., Maesano, F. E., Basili, R., Burrato, P., Carafa, M. M. C., Fracassi, U., et al. (2016). Imaging the tectonic framework of the 24 August 2016, Amatrice (central Italy) earthquake sequence: new roles for old players? *Annals of Geophysics*, 59(0). doi:<https://doi.org/10.4401/ag-7229>
- Booker, J. R. (1974). Time dependent strain following faulting of a porous medium. *Journal of Geophysical Research*, 79(14), 2037–2044. <https://doi.org/10.1029/JB079i014p02037>
- Bosl, W. J., & Nur, A. (2002). Aftershocks and pore fluid diffusion following the 1992 Landers earthquake. *Journal of Geophysical Research Solid Earth*, 107(B12), 2366. <https://doi.org/10.1029/2001JB000155>
- Brotos, V., Tomás, R., Ivorra, S., Grediaga, A., Martínez-Martínez, J., Benavente, D., et al. (2016). Improved correlation between the static and dynamic elastic modulus of different types of rocks. *Materials and Structures*, 49(8), 3021–3037. <https://doi.org/10.1617/s11527-015-0702-7>
- Bürgmann, R., & Dresen, G. (2008). Rheology of the lower crust and upper mantle: Evidence from rock mechanics, geodesy, and field observations. *Annual Review of Earth and Planetary Sciences*, 36(1), 531–567. <https://doi.org/10.1146/annurev.earth.36.031207.124326>
- Bürgmann, R., Ergintav, S., Segall, P., Hearn, E. H., McClusky, S., Reilinger, R. E., et al. (2002). Time-dependent distributed afterslip on and deep below the Izmit earthquake rupture. *Bulletin of the Seismological Society of America*, 92(1), 126–137. <https://doi.org/10.1785/0120000833>
- Calamita, F., Coltorti, M., Piccinini, D., Pierantoni, P. P., Pizzi, A., Ripepe, M., et al. (2000). Quaternary faults and seismicity in the Umbro-Marchean Apennines (central Italy): Evidence from the 1997 Colfiorito earthquake. *Journal of Geodynamics*, 29(3–5), 245–264. [https://doi.org/10.1016/S0264-3707\(99\)00054-X](https://doi.org/10.1016/S0264-3707(99)00054-X)
- Carannante, S., Monachesi, G., Cattaneo, M., Amato, A., & Chiarabba, C. (2013). Deep structure and tectonics of the northern-central Apennines as seen by regional-scale tomography and 3-D located earthquakes. *Journal of Geophysical Research: Solid Earth*, 118, 5391–5403. <https://doi.org/10.1002/jgrb.50371>
- Carminati, E., Scrocca, D., & Doglioni, C. (2010). Compaction-induced stress variations with depth in an active anticline: Northern Apennines, Italy. *Journal of Geophysical Research - Solid Earth*, 115, 1–17. <https://doi.org/10.1029/2009JB006395>
- Cheloni, D., De Novellis, V., Albano, M., Antonioli, A., Anzidei, M., Atzori, S., et al. (2017). Geodetic model of the 2016 central Italy earthquake sequence inferred from InSAR and GPS data. *Geophysical Research Letters*, 44, 6778–6787. <https://doi.org/10.1002/2017GL073580>
- Chiaraluca, L., Di Stefano, R., Tinti, E., Scognamiglio, L., Michele, M., Casarotti, E., et al. (2017). The 2016 central Italy seismic sequence: A first look at the mainshocks, aftershocks, and source models. *Seismological Research Letters*, 88(3), 757–771. <https://doi.org/10.1785/0220160221>
- Cocco, M., & Rice, J. R. (2002). Pore pressure and poroelasticity effects in Coulomb stress analysis of earthquake interactions. *Journal of Geophysical Research*, 107(B2), 2030. <https://doi.org/10.1029/2000JB000138>
- Costantini, M. (1998). A novel phase unwrapping method based on network programming. *IEEE Transactions on Geoscience and Remote Sensing*, 36(3), 813–821. <https://doi.org/10.1109/36.673674>
- Cramer, F. (2018a). Geodynamic diagnostics, scientific visualisation and StagLab 3.0. *Geoscientific Model Development*, 11(6), 2541–2562. <https://doi.org/10.5194/gmd-11-2541-2018>
- Cramer, F. (2018b). *Scientific colour-maps*. <https://doi.org/10.5281/ZENODO.1287763>
- Dieterich, J. H. (1972). Time-dependent friction in rocks. *Journal of Geophysical Research*, 77(20), 3690–3697. <https://doi.org/10.1029/JB077i020p03690>
- Dieterich, J. H. (1994). A constitutive law for rate of earthquake production and its application to earthquake clustering. *Journal of Geophysical Research*, 99(B2), 2601–2618. <https://doi.org/10.1029/93JB02581>
- Finocchio, D., Barba, S., & Basili, R. (2016). Slip rate depth distribution for active faults in central Italy using numerical models. *Tectonophysics*, 687, 232–244. <https://doi.org/10.1016/j.tecto.2016.07.031>
- Finocchio, D., Barba, S., Santini, S., & Megna, A. (2013). Interpreting the interseismic deformation of the Altotiberina fault (central Italy) through 2D modelling. *Annals of Geophysics*, 56(6). <https://doi.org/10.4401/ag-5806>
- Fyfe, W. S. (2012). *Fluids in the Earth's crust: Their significance in metamorphic, tectonic and chemical transport process*. Elsevier Science. Retrieved from <https://books.google.it/books?id=jBV6km4aNpgC>
- Gerstenberger, M. C., Wiemer, S., Jones, L. M., & Reasenberg, P. A. (2005). Real-time forecasts of tomorrow's earthquakes in California. *Nature*, 435(7040), 328–331. <https://doi.org/10.1038/nature03622>
- Gleeson, T. (2014). GLOBAL HYdrogeology MaPS (GLHYMPS) of permeability and porosity. Medford, MA. doi:<https://doi.org/10.4211/spatialdata-glyhyps>
- Gleeson, T., & Ingebritsen, S. (2012). Crustal permeability. In T. Gleeson, & S. E. Ingebritsen (Eds.). Chichester, UK: John Wiley & Sons, Ltd. <https://doi.org/10.1002/9781119166573>
- Gleeson, T., Moosdorf, N., Hartmann, J., & van Beek, L. P. H. (2014). A glimpse beneath Earth's surface: GLOBAL HYdrogeology MaPS (GLHYMPS) of permeability and porosity. *Geophysical Research Letters*, 41, 3891–3898. <https://doi.org/10.1002/2014GL059856>
- Goldstein, R. M., & Werner, C. L. (1998). Radar interferogram filtering for geophysical applications. *Geophysical Research Letters*, 25(21), 4035–4038. <https://doi.org/10.1029/1998GL900033>
- Govoni, A., Marchetti, A., De Gori, P., Di Bona, M., Lucente, F. P., Improta, L., et al. (2014). The 2012 Emilia seismic sequence (northern Italy): Imaging the thrust fault system by accurate aftershock location. *Tectonophysics*, 622, 44–55. <https://doi.org/10.1016/j.tecto.2014.02.013>
- Harris, R. A. (1998). Introduction to special section: Stress triggers, stress shadows, and implications for seismic hazard. *Journal of Geophysical Research*. <https://doi.org/10.1029/98JB01576>, 103(B10), 24,347–24,358.
- Huang, M. H., Fielding, E. J., Liang, C., Milillo, P., Bekaert, D., Dreger, D., et al. (2017). Coseismic deformation and triggered landslides of the 2016 M_w 6.2 Amatrice earthquake in Italy. *Geophysical Research Letters*, 44, 1266–1274. <https://doi.org/10.1002/2016GL071687>
- Hughes, K. L. H., Masterlark, T., & Mooney, W. D. (2010). Poroelastic stress-triggering of the 2005 $M_8.7$ Nias earthquake by the 2004 $M_9.2$ Sumatra-Andaman earthquake. *Earth and Planetary Science Letters*, 293(3–4), 289–299. <https://doi.org/10.1016/j.epsl.2010.02.043>
- ISIDe Working Group. (2016). Italian Seismological Instrumental and Parametric Data-base (ISIDe). <https://doi.org/10.13127/ISIDe>
- Jónsson, S., Segall, P., Pedersen, R., & Björnsson, G. (2003). Post-earthquake ground movements correlated to pore-pressure transients. *Nature*, 424(6945), 179–183. <https://doi.org/10.1038/nature01776>

- Jordan, T. H. (2006). Earthquake predictability, brick by brick. *Seismological Research Letters*, 77(1), 3–6. <https://doi.org/10.1785/gssrl.77.1.3>
- King, G. C. P., Stein, R. S., & Lin, J. (1995). Static stress changes and the triggering of earthquakes. *International Journal of Rock Mechanics and Mining Science and Geomechanics Abstracts*, 32(2), A50–A51. [https://doi.org/10.1016/0148-9062\(95\)94484-2](https://doi.org/10.1016/0148-9062(95)94484-2)
- Kuang, X., & Jiao, J. J. (2014). An integrated permeability-depth model for Earth's crust. *Geophysical Research Letters*, 41, 7539–7545. <https://doi.org/10.1002/2014GL061999>
- Lavecchia, G., Brozzetti, F., Barchi, M., Menichetti, M., & Keller, J. V. A. (1994). Seismotectonic zoning in east-central Italy deduced from an analysis of the Neogene to present deformations and related stress fields. *Geological Society of America Bulletin*, 106(9), 1107–1120. [https://doi.org/10.1130/0016-7606\(1994\)106<1107:SZIECI>2.3.CO;2](https://doi.org/10.1130/0016-7606(1994)106<1107:SZIECI>2.3.CO;2)
- Lavecchia, G., Castaldo, R., de Nardis, R., De Novellis, V., Ferrarini, F., Pepe, S., et al. (2016). Ground deformation and source geometry of the August 24, 2016 Amatrice earthquake (central Italy) investigated through analytical and numerical modeling of DInSAR measurements and structural-geological data. *Geophysical Research Letters*, 43, 12,389–12,398. <https://doi.org/10.1002/2016GL071723>
- Lay, T., & Kanamori, H. (1980). Earthquake doublets in the Solomon Islands. *Physics of the Earth and Planetary Interiors*, 21(4), 283–304. [https://doi.org/10.1016/0031-9201\(80\)90134-X](https://doi.org/10.1016/0031-9201(80)90134-X)
- Malagnini, L., Lucente, F. P., De Gori, P., Akinci, A., & Munafo', I. (2012). Control of pore fluid pressure diffusion on fault failure mode: Insights from the 2009 L'Aquila seismic sequence. *Journal of Geophysical Research - Solid Earth*, 117(B5), 1–15. <https://doi.org/10.1029/2011JB008911>
- Marchetti, A., Barba, S., Cucci, L., & Pirro, M. (2006). Performances of the Italian Seismic Network, 1985–2002: The hidden thing. *Annals of Geophysics*, 49(2/3), 867–879.
- Marzocchi, W., Taroni, M., & Falcone, G. (2017). Earthquake forecasting during the complex Amatrice-Norcia seismic sequence. *Science Advances*, 3(9), e1701239. <https://doi.org/10.1126/sciadv.1701239>
- Mildon, Z. K., Roberts, G. P., Faure Walker, J. P., & Iezzi, F. (2017). Coulomb stress transfer and fault interaction over millenia on non-planar active normal faults: The M_w 6.5–5.0 seismic sequence of 2016–2017, central Italy. *Geophysical Journal International*, 210(2), 1206–1218. <https://doi.org/10.1093/gji/ggx213>
- Miller, S. A., Collettini, C., Chiaraluca, L., Cocco, M., Barchi, M., & Kaus, B. J. P. (2004). Aftershocks driven by a high-pressure CO₂ source at depth. *Nature*, 427(6976), 724–727. <https://doi.org/10.1038/nature02251>
- Mirabella, F., Barchi, M. R., & Lupattelli, A. (2008). Seismic reflection data in the Umbria Marche region: Limits and capabilities to unravel the subsurface structure in a seismically active area. *Annals of Geophysics*, 51(2–3), 383–396. <https://doi.org/10.4401/ag-3032>
- MSC Software Corporation. (2016). Marc 2016 volume A: Theory and user information. Retrieved March 16, 2017, from <http://www.mscsoftware.com/it/product/marc>
- Nespoli, M., Belardinelli, M. E., Gualandi, A., Serpelloni, E., & Bonafede, M. (2018). Poroelasticity and fluid flow modeling for the 2012 Emilia-Romagna earthquakes: Hints from GPS and InSAR data. *Geofluids*, 2018, 1–15. <https://doi.org/10.1155/2018/4160570>
- Nostro, C., Chiaraluca, L., Cocco, M., Baumont, D., & Scotti, O. (2005). Coulomb stress changes caused by repeated normal faulting earthquakes during the 1997 Umbria-Marche (central Italy) seismic sequence. *Journal of Geophysical Research, B Solid Earth*, 110, 1–19. <https://doi.org/10.1029/2004JB003386>
- Nur, A., & Booker, J. R. (1972). Aftershocks caused by pore fluid flow? *Science*, 175(4024), 885–887. <https://doi.org/10.1126/science.175.4024.885>
- Ogata, Y. (1998). Space-time point-process models for earthquake occurrences. *Annals of the Institute of Statistical Mathematics*, 50(2), 379–402. <https://doi.org/10.1023/A:1003403601725>
- Papadopoulos, G. A., Ganas, A., Agalos, A., Papageorgiou, A., Triantafyllou, I., Kontoes, C., et al. (2017). Earthquake triggering inferred from rupture histories, DInSAR ground deformation and stress-transfer modelling: The case of central Italy during August 2016–January 2017. *Pure and Applied Geophysics*, 174(10), 3689–3711. <https://doi.org/10.1007/s00024-017-1609-8>
- Parsons, T., Stein, R. S., Simpson, R. W., & Reasenber, P. A. (1999). Stress sensitivity of fault seismicity: A comparison between limited-offset oblique and major strike-slip faults. *Journal of Geophysical Research*, 104(B9), 20,183–20,202. <https://doi.org/10.1029/1999JB900056>
- Peltzer, G., Rosen, P., Rogez, F., & Hudnut, K. (1998). Poroelastic rebound along the Landers 1992 earthquake surface rupture. *Journal of Geophysical Research*, 103(B12), 30,131–30,145. <https://doi.org/10.1029/98JB02302>
- Piombo, A., Martinelli, G., & Dragoni, M. (2005). Post-seismic fluid flow and Coulomb stress changes in a poroelastic medium. *Geophysical Journal International*, 162(2), 507–515. <https://doi.org/10.1111/j.1365-246X.2005.02673.x>
- Pizzi, A., Calamita, F., Coltorti, M., & Pieruccini, P. (2002). Quaternary normal faults, intramontane basins and seismicity in the Umbria-Marche-Abruzzi Apennine ridge (Italy): Contribution of neotectonic analysis to seismic hazard assessment. *Bollettino Societa'Geologica Italiana Spec. Pub.*, 1, 923–929.
- Pizzi, A., Di Domenico, A., Gallovič, F., Luzi, L., & Puglia, R. (2017). Fault segmentation as constraint to the occurrence of the main shocks of the 2016 central Italy seismic sequence. *Tectonics*, 36, 2370–2387. <https://doi.org/10.1002/2017TC004652>
- Pizzi, A., & Galadini, F. (2009). Pre-existing cross-structures and active fault segmentation in the northern-central Apennines (Italy). *Tectonophysics*, 476(1–2), 304–319. <https://doi.org/10.1016/j.tecto.2009.03.018>
- Polcari, M., Montuori, A., Bignami, C., Moro, M., Stramondo, S., & Tolomei, C. (2017). Using multi-band InSAR data for detecting local deformation phenomena induced by the 2016–2017 central Italy seismic sequence. *Remote Sensing of Environment*, 201, 234–242. <https://doi.org/10.1016/j.rse.2017.09.009>
- Reasenber, P. A., & Jones, L. M. (1989). Earthquake hazard after a mainshock in California. *Science*, 243(4895), 1173–1176. <https://doi.org/10.1126/science.243.4895.1173>
- Rice, J. R., & Cleary, M. P. (1976). Some basic stress-diffusion solutions for fluid saturated elastic porous media with compressible constituents. *Reviews of Geophysics and Space Physics*, 14(2), 227. <https://doi.org/10.1029/RG014i002p00227>
- Scholz, C. H. (1987). Wear and gouge formation in brittle faulting. *Geology*, 15(6), 493. [https://doi.org/10.1130/0091-7613\(1987\)15<493:WAGFIB>2.0.CO;2](https://doi.org/10.1130/0091-7613(1987)15<493:WAGFIB>2.0.CO;2)
- Scisciani, V., Agostini, S., Calamita, F., Pace, P., Cilli, A., Giori, I., et al. (2014). Positive inversion tectonics in foreland fold-and-thrust belts: A reappraisal of the Umbria-Marche northern Apennines (central Italy) by integrating geological and geophysical data. *Tectonophysics*, 637, 218–237. <https://doi.org/10.1016/j.tecto.2014.10.010>
- Scognamiglio, L., Margheriti, L., Mele, F. M., Tinti, E., Bono, A., De Gori, P., et al. (2012). The 2012 Pianura Padana Emiliana seismic sequence: Locations, moment tensors and magnitudes. *Annals of Geophysics*, 55(4), 549–559. <https://doi.org/10.4401/ag-6159>

- Scognamiglio, L., Tinti, E., Casarotti, E., Pucci, S., Villani, F., Cocco, M., et al. (2018). Complex fault geometry and rupture dynamics of the M_w 6.5, 30 October 2016, central Italy earthquake. *Journal of Geophysical Research: Solid Earth*, *123*, 2943–2964. <https://doi.org/10.1002/2018JB015603>
- Segall, P. (2005). *Earthquake and volcano deformation*. Princeton University Press. Hoboken, NJ, USA: John Wiley & Sons, Inc. <https://doi.org/10.1002/0471743984.vse7429>
- Serpelloni, E., Anderlini, L., & Belardinelli, M. E. (2012). Fault geometry, coseismic-slip distribution and coulomb stress change associated with the 2009 April 6, M_w 6.3, L'Aquila earthquake from inversion of GPS displacements. *Geophysical Journal International*, *188*(2), 473–489. <https://doi.org/10.1111/j.1365-246X.2011.05279.x>
- Sitharam, T. G., Sridevi, J., & Shimizu, N. (2001). Practical equivalent continuum characterization of jointed rock masses. *International Journal of Rock Mechanics and Mining Sciences*, *38*(3), 437–448. [https://doi.org/10.1016/S1365-1609\(01\)00010-7](https://doi.org/10.1016/S1365-1609(01)00010-7)
- Talwani, P., Chen, L., & Gahalaut, K. (2007). Seismogenic permeability, k_s . *Journal of Geophysical Research*, *112*, 1–18. <https://doi.org/10.1029/2006JB004665>
- Tinti, E., Scognamiglio, L., Michelini, A., & Cocco, M. (2016). Slip heterogeneity and directivity of the M_L 6.0, 2016, Amatrice earthquake estimated with rapid finite-fault inversion. *Geophysical Research Letters*, *43*, 10,745–10,752. <https://doi.org/10.1002/2016GL071263>
- Townend, J., & Zoback, M. D. (2000). How faulting keeps the crust strong. *Geology*, *28*(5), 399–402. [https://doi.org/10.1130/0091-7613\(2000\)28<399:HFKTCS>2.0.CO](https://doi.org/10.1130/0091-7613(2000)28<399:HFKTCS>2.0.CO)
- Tung, S., & Masterlark, T. (2018a). Delayed poroelastic triggering of the 2016 October Visso earthquake by the August Amatrice earthquake, Italy. *Geophysical Research Letters*, *45*, 2221–2229. <https://doi.org/10.1002/2017GL076453>
- Tung, S., & Masterlark, T. (2018b). Resolving source geometry of the 24 August 2016 Amatrice, central Italy, earthquake from InSAR data and 3D finite-element modeling. *Bulletin of the Seismological Society of America* <https://doi.org/10.1785/0120170139>, *108*(2), 553–572. Q6
- Tung, S., Masterlark, T., & Dovovan, T. (2018). Transient poroelastic stress coupling between the 2015 $M7.8$ Gorkha, Nepal earthquake and its $M7.3$ aftershock. *Tectonophysics*. <https://doi.org/10.1016/j.tecto.2018.02.003> Q7
- Utsu, T. (2002). Statistical features of seismicity. In *International geophysics series*, (pp. 719–732).
- Vadacca, L., Casarotti, E., Chiaraluce, L., & Cocco, M. (2016). On the mechanical behaviour of a low-angle normal fault: The Alto Tiberina fault (northern Apennines, Italy) system case study. *Solid Earth*, *7*(6), 1537–1549. <https://doi.org/10.5194/se-7-1537-2016>
- Valoroso, L., Chiaraluce, L., Piccinini, D., Di Stefano, R., Schaff, D., & Waldhauser, F. (2013). Radiography of a normal fault system by 64,000 high-precision earthquake locations: The 2009 L'Aquila (central Italy) case study. *Journal of Geophysical Research: Solid Earth*, *118*, 1156–1176. <https://doi.org/10.1002/jgrb.50130>
- Walters, R. J., Gregory, L. C., Wedmore, L. N. J., Craig, T. J., McCaffrey, K., Wilkinson, M., et al. (2018). Dual control of fault intersections on stop-start rupture in the 2016 central Italy seismic sequence. *Earth and Planetary Science Letters*, *500*, 1–14. <https://doi.org/10.1016/j.epsl.2018.07.043>
- Wang, H. (2000). *Theory of linear poroelasticity with applications to geomechanics and hydrogeology*. Princeton University Press.
- Wegmuller, U., & Werner, C. (1997). Gamma SAR processor and interferometry software. In *ERS symposium on space at the service of our environment*, (pp. 1687–1692). Florence: ESA Publications Division.